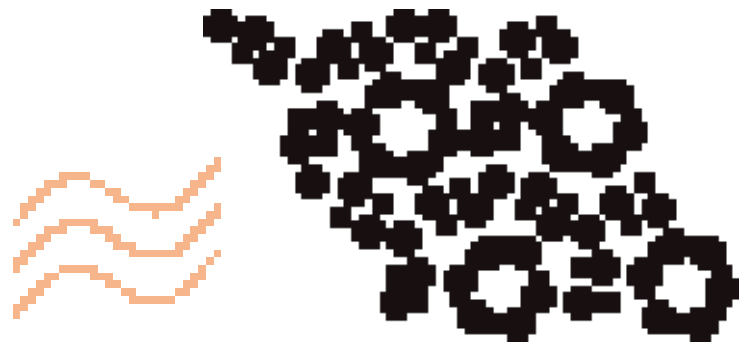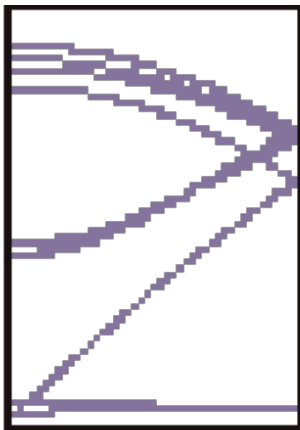Longitudinal acoustic phonons used out-of-plane heat conduction!

It's not very effective...

The Path To Relaxation

Understanding thermal conduction in twisted stacks
with non-equilibrium phonon dynamics

Master's thesis in Physics

Patrik Wallin Hybelius

Master's thesis 2022

The Path To Relaxation

Understanding thermal conduction in twisted stacks
with non-equilibrium phonon dynamics

Patrik Wallin Hybelius

The Path To Relaxation
Understanding thermal conduction in twisted stacks
with non-equilibrium phonon dynamics
Patrik Wallin Hybelius

Cover: Allusion to the Pokémon video games, highlighting the inefficiency of out-of-plane thermal transport in twisted stacks of van-der-Waals thin films.

The Path To Relaxation
Understanding thermal conduction in twisted stacks
with non-equilibrium phonon dynamics
Patrik Wallin Hybelius
Department of Physics
Chalmers University of Technology

Abstract

In this work, the details of thermal transport in graphite is studied. The aim is to understand a striking anisotropy observed in the thermal conductivity of twisted stacks of van-der-Waals thin sheets, as well as to explore the limitations of the relaxation time approximation of the Boltzmann transport equation. To this end, classical molecular dynamics simulations were performed, and analyzed using projection onto phonon modes. Atomic forces were modeled using neuroevolution potentials previously trained on results from density functional theory, and GPUMD was used to run simulations on graphical processing units. Phonon modes were defined from Second-order force constants extracted from the neuroevolution potential using HIPHIVE. The simulations were done both in equilibrium and in variations of non-equilibrium. The equilibrium phonons were modeled using Langevin dynamics to extract their lifetimes and finite-temperature renormalized frequencies. Non-equilibrium states were studied by exciting individual out-of-plane modes to extreme amplitudes before running the simulations, and then following the energy as it was distributed from the pumped modes to the rest of the system. Contrary to the exponential decay predicted by the relaxation time approximation, energy was observed to oscillate back and forth between modes when initially excited to a sufficient degree. Furthermore, the system was observed to reach a long-lived quasi-equilibrium state, where a set of coupled modes collectively retained an above-equilibrium energy for an extended period of time. The quasi-equilibrium lifetime was found to depend negatively on the size of the simulated system, but the limit at large sizes remains unknown.

Acknowledgements

I would like to thank my supervisor and examiner Paul Erhart for giving me the opportunity to write this thesis. Your enthusiasm is inspiring and I sincerely hope I get the chance to discuss physics with you again in the future.

I would also like to sincerely thank everyone at the Computational Materials group at Chalmers for creating such a welcoming and warm atmosphere. In particular, I am grateful to my supervisor Erik Fransson for all our fruitful discussions, and to Fredrik Eriksson for your insight and coding expertise.

I additionally want to express my gratitude my friend and opponent Olof Cronquist for all the coffee breaks and discussions over the course of the semester.

Finally, I want to thank Frida Wallin Hybelius and the rest of my family for supporting me throughout my studies, and my friends for turning the last five years into memories I will carry fondly for the rest of my life.

<div align="center">Patrik Wallin Hybelius, Gothenburg, October 2022</div>

Glossary

BTE Boltzmann transport equation. 2, 7
BZ Brillouin zone. 14, 16, 17, 20, 26

DFT density functional theory. 2, 5, 20–22

FC force constant. 3, 5, 8, 20, 21, 23, 24, 37
FCP force constant potential. 5, 20, 23, 24

GPU graphical processing unit. 19, 20

LA longitudinal acoustic. 24–33, 35–38
LBTE linearized Boltzmann equation. 8, 10, 35
LO longitudinal optical. 31, 38
LTC lattice thermal conductivity. 1, 2, 5, 11, 37, 38

MD molecular dynamics. 5, 6, 11, 12, 14, 19–21, 26, 28, 30, 34, 35, 37

NEP neuroevolution potential. 5, 20–23

RTA relaxation time approximation. 2, 10, 31, 38

TA transverse acoustic. 24–26, 31–33, 38
TMD transition metal dichalcogenide. 1, 19
TO transverse optical. 27–36

vdW van-der-Waals. 1, 2, 37, 38

Contents

Contents

List of Figures

1
Introduction

1.1 Background

In the development of higher performing computer hardware, circuits are reducing in size to the point where fulfilling Moore's law becomes increasingly challenging [1]. In order to keep increasing performance despite the difficulty in further size reduction, manufacturers are moving towards increasingly complex transistor and circuit structures [22]. This creates a demand for fine-tunable thermal management able to deal with highly heterogeneous temperature profiles at the die level [24].

A recent study demonstrated the possibility to construct materials with extremely anisotropic thermal conductivity by stacking randomly rotated van-der-Waals (vdW) thin films consisting of transition metal dichalcogenides (TMDs) such as MoS_2 [19]. Such materials could enable highly controlled heat management at the nanometer level. The study showed that such stacks of MoS_2 films exhibit high in-plane thermal conductivity due to the crystallinity within each layer, and simultaneously possess low through-plane conductivity caused by the random stacking angles leading to glass-like transport properties.

1.2 Aim

The aim of this thesis is to build on the results of Kim *et al.* [19] by studying the effects of twist angle and materials choice on the in-plane and through-plane thermal conductivities. Furthermore, specific mechanisms of thermal conduction are to be investigated by looking at phonon relaxation paths and lifetimes.

1.3 Limitations

Since the inclusion of the electronic contribution to the thermal conductivity would drastically increase the complexity of the problem due to electron-phonon interactions, and since the lattice thermal conductivity (LTC) is the dominant contribution in the materials of interest [25], electron dynamics will not be included in the analysis or simulations. Similarly, impurities and in-plane structural boundaries, which are unavoidable in experiments and real-world realizations of the materials under consideration, will be neglected here since they are not directly related to the phenomena of interest. Regarding the realism of the simulations, two additional limitations come into play. Firstly, the model to be used is built to approximate

the energy landscape described by density functional theory (DFT) using a specific functional. Regardless of the limitations of DFT, however, the results should be in qualitative agreement with reality, and the correct mechanisms of phonon interactions should be incorporated. Secondly, many of the simulations to be performed are based on classical physics and will thus disregard quantum effects. Still, the most relevant phenomena for the considered systems at finite temperatures are expected to be captured through the use of Bose-Einstein statistics.

1.4 Specification of issue under investigation

Three main objectives underlie this thesis. The first goal is to find an optimal twist angle between atomic layers that minimizes the through-plane LTC for the considered materials. While it would be possible to accomplish this by simulating heat conduction in a selection of systems with various twist angles, a more enlightening approach is to attempt to find an optimum on a theoretical basis. Therefore, the second goal is to provide physical insight into the mechanisms behind the reduction of the through-plane LTC in twisted vdW thin film stacks compared to the untwisted counterparts. One of the more common theories of crystalline thermal transport is the Boltzmann transport equation (BTE) in the relaxation time approximation (RTA). The RTA relates the LTC in a system near equilibrium to phonon mode lifetimes and group velocities, under the assumption that phonons in different modes decay independently [29]. In glasses, however, the RTA tends to perform poorly [26]. Therefore, since the low through-plane thermal conductivity observed by Kim *et al.* [19] is attributed to glass-like thermal transport, the applicability of the RTA in the present cases is put into question. For this reason, the third goal is to examine the suitability of the RTA in describing the LTC of the considered systems. This goal will be accomplished by directly simulating the relaxation of individual phonon modes excited far beyond equilibrium, outside the regime of the RTA. Furthermore, these simulations have an experimental analogue where specific modes can be excited in a sample by the use of laser pulses of appropriate frequency [15], meaning the results produced here will be experimentally testable.

2

Theory

2.1 Phonons

For a given system satisfying the Born-Oppenheimer approximation, the lattice part of the Hamiltonian is given by

$$\mathcal{H} = \sum_{n\mu} \frac{\boldsymbol{p}_\mu^2}{2m_{n\mu}} + U(\{\boldsymbol{R}_{n\mu}\}), \tag{2.1}$$

where n and μ are the unit cell and site indices, respectively. The first term is the kinetic energy and the second term describes the potential energy for a set of atom positions $\boldsymbol{R}_{n\mu} = \boldsymbol{R}_n + \boldsymbol{r}_\mu$, where $\boldsymbol{R}_n$ denotes the origin of unit cell n and $\boldsymbol{r}_\mu$ is the position of atom μ in the unit cell. Taylor expanding the potential energy around $\boldsymbol{R}_{n\mu}^0$ gives

$$
\begin{aligned}
U &= \sum_{n\mu\alpha} \Phi_{n\mu}^\alpha u_{n\mu}^\alpha + \frac{1}{2!} \sum_{n\mu\alpha} \sum_{n'\mu'\alpha'} \Phi_{nn'\mu\mu'}^{\alpha\alpha'} u_{n\mu}^\alpha u_{n'\mu'}^{\alpha'} \\
&\quad + \frac{1}{3!} \sum_{n\mu\alpha} \sum_{n'\mu'\alpha'} \sum_{\substack{n''\mu''\alpha'' \\ \mu\mu'\mu''}} \Phi_{nn'n''}^{\alpha\alpha'\alpha''} u_{n\mu}^\alpha u_{n'\mu'}^{\alpha'} u_{n''\mu''}^{\alpha''} + \dots \\
&= \sum_{n\mu\alpha} \left(\Phi_{n\mu}^\alpha u_{n\mu}^\alpha + \frac{1}{2!} \sum_{n'\mu'\alpha'} \Phi_{nn'\mu\mu'}^{\alpha\alpha'} u_{n\mu}^\alpha u_{n'\mu'}^{\alpha'} \right. \tag{2.2} \\
&\qquad \left. + \frac{1}{3!} \sum_{n'\mu'\alpha'} \sum_{\substack{n''\mu''\alpha'' \\ \mu\mu'\mu''}} \Phi_{nn'n''}^{\alpha\alpha'\alpha''} u_{n\mu}^\alpha u_{n'\mu'}^{\alpha'} u_{n''\mu''}^{\alpha''} + \dots \right) \\
&= \sum_{n\mu} U_{n\mu},
\end{aligned}
$$

where $\boldsymbol{u}_{n\mu} = \boldsymbol{R}_{n\mu} - \boldsymbol{R}_{n\mu}^0$ and Φ are the force constants (FCs), defined as the partial derivatives of U with respect to $\boldsymbol{u}_{n\mu}$. The superscripts α denote cartesian directions and are used to accurately express scalar products, $\boldsymbol{u}_{n\mu} \cdot \boldsymbol{u}_{n'\mu'} = \sum_\alpha u_{n\mu}^\alpha u_{n'\mu'}^\alpha$. In the last line, $U_{n\mu}$ is the potential energy of atom $(n\mu)$, although this is not the only way to define it. The energy is taken to be zero at $\boldsymbol{u}_{n\mu} = 0$, and by selecting $\boldsymbol{R}_{n\mu}^0$ to be the atom positions at rest, i.e., a minimum of U, the first order terms can be dropped. Truncating U at the second-order (harmonic) term gives $\mathcal{H}$ in the form of

a set of coupled harmonic oscillators

$$
\begin{aligned}
\mathcal{H}_{\text{harm}} = \; & \frac{1}{2} \sum_{n\mu\alpha} \frac{(p_{n\mu}^{\alpha})^2}{m_\mu} \\
& + \frac{1}{2} \sum_{n\mu\alpha} \sum_{n'\mu'\alpha'} \Phi_{nn'\mu\mu'}^{\alpha\alpha'} u_{n\mu}^{\alpha} u_{n'\mu'}^{\alpha'}.
\end{aligned}
\tag{2.3}
$$

Phonon modes and frequencies are given as eigenfunctions to this Hamiltonian, expressed as

$$
\omega_{\boldsymbol{q}j}^2 A_{\mu j}^{\alpha}(\boldsymbol{q}) = \sum_{\mu'\alpha'} D_{\mu\mu'}^{\alpha\alpha'}(\boldsymbol{q}) A_{\mu'j}^{\alpha'}(\boldsymbol{q})
\tag{2.4}
$$

with the dynamical matrix

$$
D_{\mu\mu'}^{\alpha\alpha'}(\boldsymbol{q}) = \frac{1}{N} \frac{1}{\sqrt{m_\mu m_{\mu'}}} \sum_{nn'} \Phi_{nn'\mu\mu'}^{\alpha\alpha'} e^{-i\boldsymbol{q}\cdot(\boldsymbol{R}_n - \boldsymbol{R}_{n'})},
\tag{2.5}
$$

eigenfunctions $A_{\mu j}^{\alpha}(\boldsymbol{q})$ and crystal momentum vector $\boldsymbol{q}$. Upon normalization the eigenfunctions naturally form a complete and orthonormal basis set,

$$
\sum_{\mu\mu'} \sum_{\alpha\alpha'} A_{\mu j}^{\alpha *} A_{\mu'j'}^{\alpha'} = \delta_{jj'},
\tag{2.6}
$$

and can thus be used to express $u_{n\mu}^{\alpha}$ in terms of normal coordinates

$$
u_{n\mu}^{\alpha} = \frac{1}{\sqrt{N}} \frac{1}{\sqrt{m_\mu}} \sum_{\boldsymbol{q}j} A_{\mu j}^{\alpha}(\boldsymbol{q}) e^{i\boldsymbol{q}\cdot\boldsymbol{R}_n^0} Q_j(\boldsymbol{q}),
\tag{2.7}
$$

with the inverse

$$
Q_j(\boldsymbol{q}) = \frac{1}{\sqrt{N}} \sum_{n\mu\alpha} \sqrt{m_\mu} A_{\mu j}^{\alpha *}(\boldsymbol{q}) e^{-i\boldsymbol{q}\cdot\boldsymbol{R}_n^0} u_{n\mu}^{\alpha}.
\tag{2.8}
$$

Here, N is the number of unit cells and j enumerates the eigenvectors of $D_{\mu\mu'}^{\alpha\alpha'}(\boldsymbol{q})$. Since the dynamical matrix at $\boldsymbol{q}$ has shape $3p \times 3p$, where p is the number of atoms in a unit cell, there is $3p$ eigenvectors, each corresponding to a so-called phonon band. Hence, j is referred to as the band index. The conjugate momentum

$$
\Pi_j(\boldsymbol{q}) = \dot{Q}_j(\boldsymbol{q})
\tag{2.9}
$$

can be defined similarly. This enables a compact expression of the harmonic Hamiltonian

$$
\mathcal{H}_{\text{harm}} = \frac{1}{2} \sum_{\boldsymbol{q}j} \left(\Pi_j^*(\boldsymbol{q}) \Pi_j(\boldsymbol{q}) + \omega_j^2(\boldsymbol{q}) Q_j^*(\boldsymbol{q}) Q_j(\boldsymbol{q}) \right).
\tag{2.10}
$$

Some symmetries between $\boldsymbol{q}$ and $-\boldsymbol{q}$ can be identified here, namely

$$
\begin{aligned}
Q_j^*(\boldsymbol{q}) &= Q_j(-\boldsymbol{q}), \\
\Pi_j^*(\boldsymbol{q}) &= \Pi_j(-\boldsymbol{q}), \\
\omega_j(\boldsymbol{q}) &= \omega_j(-\boldsymbol{q}), \\
\boldsymbol{v}_j(\boldsymbol{q}) &= -\boldsymbol{v}_j(-\boldsymbol{q}),
\end{aligned}
\tag{2.11}
$$

where $\boldsymbol{v}_j(\boldsymbol{q}) = \nabla_{\boldsymbol{q}}\omega_j(\boldsymbol{q})$ is the group velocity. Interpreting $Q_j(\boldsymbol{q})$ and $\Pi_j(\boldsymbol{q})$ as operators lets us define phonon annihilation and creation operators

$$b_{\boldsymbol{q}j} = \sqrt{\frac{\omega_j(\boldsymbol{q})}{2\hbar}}Q_j(\boldsymbol{q}) + i\sqrt{\frac{1}{2\hbar\omega_j(\boldsymbol{q})}}\Pi_j(-\boldsymbol{q})$$

$$b_{\boldsymbol{q}j}^{\dagger} = \sqrt{\frac{\omega_j(\boldsymbol{q})}{2\hbar}}Q_j(-\boldsymbol{q}) - i\sqrt{\frac{1}{2\hbar\omega_j(\boldsymbol{q})}}\Pi_j(\boldsymbol{q}),$$

(2.12)

which fulfill bosonic commutation relations

$$[b_{\boldsymbol{q}j}, b_{\boldsymbol{q}'j'}] = [b_{\boldsymbol{q}j}^{\dagger}, b_{\boldsymbol{q}'j'}^{\dagger}] = 0$$

$$[b_{\boldsymbol{q}j}, b_{\boldsymbol{q}'j'}^{\dagger}] = \delta_{\boldsymbol{q}\boldsymbol{q}'}\delta_{jj'}$$

(2.13)

and enable a final simplification of the harmonic Hamiltonian

$$\mathcal{H}_{\text{harm}} = \sum_{\lambda} \hbar\omega_{\lambda}\left(b_{\lambda}^{\dagger}b_{\lambda} + \frac{1}{2}\right) = \sum_{\lambda} \hbar\omega_{\lambda}\left(n_{\lambda} + \frac{1}{2}\right),$$

(2.14)

where $\lambda = \boldsymbol{q}j$ is a composite index and $n_{\lambda} = b_{\lambda}^{\dagger}b_{\lambda}$ is the phonon mode occupation number operator [32].

2.2 Molecular dynamics

Molecular dynamics (MD) simulations is a method for (usually classically) simulating the time evolution of a system to calculate properties such as the LTC. To this end, the potential energy $U(\boldsymbol{R}_{n,\mu})$ needs to be described by some model. Two models will be used in this thesis. Firstly, we will use force constant potentials (FCPs), which are obtained by fitting the FCs in Eq. (2.2) directly to DFT results. Secondly, we will employ the neuroevolution potential (NEP) approach [14], which represents $U(\boldsymbol{R}_{n,\mu})$ using a neural network trained on DFT data. In either case, the model is used to evaluate atomic forces [4]

$$F_{n\mu}^{\alpha} = -\frac{\partial U}{\partial u_{n\mu}^{\alpha}},$$

(2.15)

which are in turn used to evolve the system in time by integrating the equations of motion

$$\dot{u}_{n\mu}^{\alpha} = \frac{\partial H}{\partial p_{n\mu}^{\alpha}} = \frac{p_{n\mu}^{\alpha}}{m_{n\mu}}$$

$$\dot{p}_{n\mu}^{\alpha} = -\frac{\partial H}{\partial u_{n\mu}^{\alpha}} = F_{n\mu}^{\alpha}.$$

(2.16)

The integration is commonly done via the velocity Verlet algorithm [27], where particle positions and velocities are updated at some time step interval Δt according to

$$\boldsymbol{v}_{n\mu,i}' = \boldsymbol{v}_{n\mu,i} + \frac{1}{2}\frac{\boldsymbol{F}_{n\mu,i}}{m_{n\mu}}\Delta t$$

$$\boldsymbol{u}_{n\mu,i+1} = \boldsymbol{u}_{n\mu,i} + \boldsymbol{v}_{n\mu,i}'\Delta t$$

$$\boldsymbol{v}_{n\mu,i+1} = \boldsymbol{v}_{n\mu,i}' + \frac{1}{2}\frac{\boldsymbol{F}_{n\mu,i+1}}{m_{n\mu}}\Delta t,$$

(2.17)

where $\boldsymbol{v}_{n\mu,i}$ and $\boldsymbol{v}_{n\mu,i}$ are positions and velocities at time $t = t_0 + i\Delta t$ and $\boldsymbol{v}'_{n\mu,i}$ is the intermediate velocity at time $t = t_0 + (i + 1/2)\Delta t$.

Simulating a system as described above naturally preserves the number of particles, the system volume, and the total energy due to conservation laws fulfilled by the classical equations of motion, be it in the form of Newton, Euler-Lagrange or Hamiltonian. In other words, the simulation describes a system in the microcanonical (NVE) ensemble. However, for the quantities of interest here, it is necessary to control the system temperature rather than the total energy. A system where the number of particles, volume and temperature are conserved is said to be in the canonical (NVT) ensemble. Likewise, if the number of particle, pressure and temperature are conserved the system is said to be in the isothermal-isobaric (NPT) ensemble.

To preserve the temperature during MD simulation, a thermostat needs to be introduced, which controls the particle velocities such that the equipartition theorem is fulfilled on average,

$$\sum_{n\mu} \frac{1}{2} m_\mu v_{n\mu}^2 = \frac{3}{2} pNk_BT. \tag{2.18}$$

One common class of thermostats are velocity rescaling methods, perhaps the most advanced of which is the Bussi-Donadio-Parrinelo thermostat [5, 3]. In the simplest version of this thermostat, at the end of each time step, the velocities are rescaled such that the total kinetic energy K equals a target K_t, which is a stochastic variable drawn from the probability distribution of the total kinetic energy in a canonical ensemble in equilibrium at some temperature T. That is, the velocities are updated as follows

$$\begin{aligned} \boldsymbol{v}_{n\mu} &\to \alpha \boldsymbol{v}_{n\mu}, \quad \text{where} \\ \alpha &= \sqrt{\frac{K_t}{K}}, \\ K &= \sum_{n,\mu} \frac{1}{2} m_{n\mu} v_{n\mu}^2, \\ P(K_t) &\propto K_t^{3pN-1} e^{-K_t/k_BT}. \end{aligned} \tag{2.19}$$

The method can also be adapted to update velocities more smoothly by using a thermostat time parameter and letting K_t depend on K [5].

Another thermostat, not based on velocity rescaling, is the Nosé-Hoover chain method, which uses additional degrees of freedom to model a heat bath [23]. Hamilton's equations are extended to include a chain of M heat bath variables ζ_i with

masses Q_i according to

$$
\begin{aligned}
\dot{\boldsymbol{u}}_{n\mu} &= \boldsymbol{p}_{n\mu} \\
\dot{\boldsymbol{p}}_{n\mu} &= \boldsymbol{F}_{n\mu} - \boldsymbol{p}_{n\mu}\frac{\zeta_1}{Q_1} \\
\dot{\zeta_1} &= \sum_{n\mu}\frac{\boldsymbol{p}_{n\mu}^2}{m_{n\mu}} - pNk_BT - \zeta_1\frac{\zeta_2}{Q_2} \\
\dot{\zeta_i} &= \frac{\zeta_{i-1}^2}{Q_{i-1}} - k_BT - \zeta_i\frac{\zeta_{i+1}}{Q_{i+1}}, \quad 1 < i < M \\
\dot{\zeta_M} &= \frac{\zeta_{M-1}^2}{Q_{M-1}} - k_BT.
\end{aligned}
\tag{2.20}
$$

The thermostat used in the present work is based on Langevin dynamics, which can be considered a modification of the classical equations of motion by inclusion of a friction term and a term modeling random collisions between particles,

$$
\begin{aligned}
\dot{\boldsymbol{u}}_{n\mu} &= \boldsymbol{p}_{n\mu} \\
\dot{\boldsymbol{p}}_{n\mu} &= \boldsymbol{F}_{n\mu} - \gamma\boldsymbol{p}_{n\mu} + \sqrt{2m_\mu k_BT}\,\boldsymbol{W}(t),
\end{aligned}
\tag{2.21}
$$

where γ is a friction coefficient and $\boldsymbol{W}(t)$ is a three-dimensional stochastic variable of mean zero, normalized such that $\langle \boldsymbol{W}(t)\cdot\boldsymbol{W}(t')\rangle = \delta(t-t')$ [6].

2.3 Boltzmann transport

In Boltzmann transport theory, the phonon mode occupation numbers are represented by a distribution function $n_\lambda(t)$ giving the average number of phonons in mode λ at time t. The evolution of this distribution in time is governed by diffusion and scattering, and is described by the BTE [32]

$$
\frac{\partial n_\lambda}{\partial t} + \boldsymbol{v}_\lambda \cdot \frac{\partial n_\lambda}{\partial \boldsymbol{r}} = \left.\frac{\partial n_\lambda}{\partial t}\right|_c.
\tag{2.22}
$$

The second term on the left is the diffusion term, and in the case of the thermal conductivity the spatial dependence of n_λ originates from a temperature gradient, whence

$$
\frac{\partial n_\lambda}{\partial \boldsymbol{r}} = \frac{\partial n_\lambda}{\partial T}\nabla T.
\tag{2.23}
$$

The term on the right is the scattering or collision term, describing interactions between phonons where energy and momentum is transferred between modes. There are no such interactions in the harmonic picture, so in order for the BTE to be useful for phonon dynamics, some anharmonic terms need to be kept in the potential energy expansion. Normally, the third-order terms, corresponding to three-particle interactions, are kept while higher order terms are discarded. This is done because the number of n-particle interaction terms increases combinatorially with n, while their magnitudes tend to decrease even faster. Hence there is a high cost and (often) low gain in keeping higher-order terms. The BTE is usually solved via linearization

$$
n_\lambda(t) = n_\lambda^0 + n_\lambda^1(t).
$$

Here, n_λ^0 is the time-independent equilibrium solution, given by the Bose-Einstein distribution

$$n_\lambda^0 = \frac{1}{e^{\hbar\omega_\lambda/k_B T} - 1},$$

which does not contribute to the collision term. The collision term caused by anharmonic interactions as well as the temperature gradient ∇T are treated as perturbations, giving rise to a change in the phonon distribution that is linear in time, $n_\lambda^1(t)$. The linearized Boltzmann equation (LBTE) becomes, upon dropping second order perturbation terms,

$$\frac{\partial n_\lambda^1}{\partial t} + \boldsymbol{v}_\lambda \cdot \nabla T \frac{\partial n_\lambda^0}{\partial T} = \left.\frac{\partial n_\lambda^1}{\partial t}\right|_c. \tag{2.24}$$

The collision term can be expressed in terms of the third-order FCs and phonon eigenfunctions [32, 29, 8] by using Fermi's golden rule

$$\left.\frac{\partial n_\lambda^1}{\partial t}\right|_c = \Gamma_\lambda^{\text{in}} - \Gamma_\lambda^{\text{out}},$$

where $\Gamma_\lambda^{\text{in}}$ and $\Gamma_\lambda^{\text{out}}$ are total scattering rates into and out of mode λ given by

$$\Gamma_\lambda^{\text{in}} = \sum_{\lambda'\lambda''} \left((1+n_\lambda)(1+n_{\lambda'})n_{\lambda''} P_{\lambda''}^{\lambda\lambda'} + \frac{1}{2}(1+n_\lambda)n_{\lambda'}n_{\lambda''} P_{\lambda'\lambda''}^{\lambda} \right)$$

and

$$\Gamma_\lambda^{\text{out}} = \sum_{\lambda'\lambda''} \left(n_\lambda n_{\lambda'}(1+n_{\lambda''}) P_{\lambda\lambda'}^{\lambda''} + \frac{1}{2}n_\lambda(1+n_{\lambda'})(1+n_{\lambda''}) P_{\lambda}^{\lambda'\lambda''} \right).$$

Here, $P_{\lambda\lambda'}^{\lambda''}$ is the intrinsic scattering rate of λ with λ' under formation of λ'' and $P_{\lambda}^{\lambda'\lambda''}$ is the decay rate of λ into λ' and λ''. The scattering rates are given by

$$P_{\lambda\lambda'}^{\lambda''} = \frac{2\pi}{\hbar^2}|\Phi_{\lambda\lambda'-\lambda''}|^2 \delta(\omega_\lambda + \omega_{\lambda'} - \omega_{\lambda''})$$

and

$$P_{\lambda}^{\lambda'\lambda''} = \frac{2\pi}{\hbar^2}|\Phi_{\lambda-\lambda'-\lambda''}|^2 \delta(\omega_\lambda - \omega_{\lambda'} - \omega_{\lambda''}),$$

where $\Phi_{\lambda\lambda'\lambda''}$ is the Fourier representation of the third-order force constants

$$\begin{aligned}
\Phi_{\lambda\lambda'\lambda''} = &\frac{1}{\sqrt{N}} \sum_{\mu\alpha} \sum_{\mu'\alpha'} \sum_{\mu''\alpha''} A_{\mu j}^{\alpha} A_{\mu'j'}^{\alpha'} A_{\mu''j''}^{\alpha''} \sqrt{\frac{\hbar}{2m_\mu\omega_\lambda}} \sqrt{\frac{\hbar}{2m_{\mu'}\omega_{\lambda'}}} \sqrt{\frac{\hbar}{2m_{\mu''}\omega_{\lambda''}}} \\
&\times \sum_{\substack{n'n'' \\ \mu\mu'\mu''}} \Phi_{nn'n''}^{\alpha\alpha'\alpha''} e^{-i\boldsymbol{q}'\cdot\boldsymbol{R}_{n'\mu'}^0} e^{-i\boldsymbol{q}''\cdot\boldsymbol{R}_{n''\mu''}^0} \Delta(\boldsymbol{q}+\boldsymbol{q}'+\boldsymbol{q}'').
\end{aligned} \tag{2.25}$$

In the final line, $\Delta(\boldsymbol{q}+\boldsymbol{q}'+\boldsymbol{q}'')$ is one if $\boldsymbol{q}+\boldsymbol{q}'+\boldsymbol{q}''$ is a reciprocal lattice vector and zero otherwise. This ensures conservation of crystal momentum, while the delta functions $\delta(\cdot)$ in $P_{\lambda\lambda'}^{\lambda''}$ and $P_{\lambda}^{\lambda'\lambda''}$ ensure conservation of energy. By assumption, the collision term is zero in equilibrium, which means contributions to $\Gamma_\lambda^{\text{in}}$ and $\Gamma_\lambda^{\text{out}}$ from

n_λ^0 cancel to zero. Hence, the two scattering rates can be expressed more compactly as

$$\Gamma_\lambda^{\text{in}} = n_\lambda^1 \sum_{\lambda'\lambda''} \left((1+n_{\lambda'})n_{\lambda''} P_{\lambda''}^{\lambda\lambda'} + \frac{1}{2} n_{\lambda'} n_{\lambda''} P_{\lambda'\lambda''}^{\lambda} \right)$$

and

$$\Gamma_\lambda^{\text{out}} = n_\lambda^1 \sum_{\lambda'\lambda''} \left(n_{\lambda'}(1+n_{\lambda''}) P_{\lambda\lambda'}^{\lambda''} + \frac{1}{2}(1+n_{\lambda'})(1+n_{\lambda''}) P_{\lambda}^{\lambda'\lambda''} \right).$$

Furthermore, due to symmetries in $\Psi_{\lambda\lambda'\lambda''}$, the terms in $\Gamma_\lambda^{\text{in}}$ and $\Gamma_\lambda^{\text{out}}$ can be conveniently factored by expressing the intrinsic scattering rates as

$$P_{\lambda''}^{\lambda\lambda'} = \frac{2\pi}{\hbar} |\Psi_{-\lambda\lambda'\lambda''}|^2 \delta(\omega_\lambda + \omega_{\lambda'} - \omega_{\lambda''})$$

$$P_{\lambda'\lambda''}^{\lambda} = \frac{2\pi}{\hbar} |\Psi_{-\lambda\lambda'\lambda''}|^2 \delta(\omega_\lambda - \omega_{\lambda'} - \omega_{\lambda''})$$

$$P_{\lambda\lambda'}^{\lambda''} = \frac{2\pi}{\hbar} |\Psi_{-\lambda\lambda'\lambda''}|^2 \delta(\omega_\lambda + \omega_{\lambda'} - \omega_{\lambda''})$$

$$P_{\lambda}^{\lambda'\lambda''} = \frac{2\pi}{\hbar} |\Psi_{-\lambda\lambda'\lambda''}|^2 \delta(\omega_\lambda - \omega_{\lambda'} - \omega_{\lambda''}).$$

Combining the sums in $\Gamma_\lambda^{\text{in}}$ and $\Gamma_\lambda^{\text{out}}$, we get

$$\Gamma_\lambda^{\text{in}} - \Gamma_\lambda^{\text{out}} =$$

$$\frac{2\pi}{\hbar^2} n_\lambda^1 \sum_{\lambda'\lambda''} |\Psi_{-\lambda\lambda'\lambda''}|^2 \Bigg[\Big((1+n_{\lambda'})n_{\lambda''} - n_{\lambda'}(1+n_{\lambda''})\Big)\delta(\omega_\lambda + \omega_{\lambda'} - \omega_{\lambda''})$$

$$+ \frac{1}{2}\Big(n_{\lambda'}n_{\lambda''} - (1+n_{\lambda'})(1+n_{\lambda''})\Big)\delta(\omega_\lambda - \omega_{\lambda'} - \omega_{\lambda''}) \Bigg] =$$

$$\frac{2\pi}{\hbar^2} n_\lambda^1 \sum_{\lambda'\lambda''} |\Psi_{-\lambda\lambda'\lambda''}|^2 \Bigg[(n_{\lambda''} - n_{\lambda'})\delta(\omega_\lambda + \omega_{\lambda'} - \omega_{\lambda''})$$

$$- \frac{1}{2}(1 + n_{\lambda'} + n_{\lambda''})\delta(\omega_\lambda - \omega_{\lambda'} - \omega_{\lambda''}) \Bigg].$$

Finally, since the summation includes each pair λ', λ'' twice in opposite orders, it can be made more symmetrical by replacing

$$(n_{\lambda''} - n_{\lambda'})\delta(\omega_\lambda + \omega_{\lambda'} - \omega_{\lambda''})$$

with

$$\frac{1}{2}(n_{\lambda''} - n_{\lambda'})\delta(\omega_\lambda + \omega_{\lambda'} - \omega_{\lambda''}) + \frac{1}{2}(n_{\lambda'} - n_{\lambda''})\delta(\omega_\lambda - \omega_{\lambda'} + \omega_{\lambda''}) =$$

$$\frac{1}{2}(n_{\lambda''} - n_{\lambda'})\Big(\delta(\omega_\lambda + \omega_{\lambda'} - \omega_{\lambda''}) - \delta(\omega_\lambda - \omega_{\lambda'} + \omega_{\lambda''})\Big),$$

giving

$$\Gamma_\lambda^{\text{in}} - \Gamma_\lambda^{\text{out}} = -\frac{\pi}{\hbar^2} n_\lambda^1 \sum_{\lambda'\lambda''} |\Psi_{-\lambda\lambda'\lambda''}|^2 \Bigg[(1 + n_{\lambda'} + n_{\lambda''})\delta(\omega_\lambda - \omega_{\lambda'} - \omega_{\lambda''})$$

$$+ (n_{\lambda'} - n_{\lambda''})\Big(\delta(\omega_\lambda + \omega_{\lambda'} - \omega_{\lambda''}) - \delta(\omega_\lambda - \omega_{\lambda'} + \omega_{\lambda''})\Big) \Bigg].$$

$$(2.26)$$

A simpler approximation to the collision term in Eq. (2.24) is the RTA

$$\left.\frac{\partial n_\lambda^1}{\partial t}\right|_c = -\frac{n_\lambda^1}{\tau_\lambda}.$$

Intuitively, this means the specific phonon mode interactions are smoothed out, and each mode is instead assumed to relax on a constant time scale τ_λ due to interaction with a reservoir consisting of all the other modes. An expression for the relaxation time or lifetime, in the case of scattering described by third-order force constants, can be acquired by comparing $\left.\frac{\partial n_\lambda^1}{\partial t}\right|_c$ as given by the RTA with the one given by Fermi's golden rule.

$$\frac{1}{\tau_\lambda} = \frac{\Gamma_\lambda^{\text{out}} - \Gamma_\lambda^{\text{in}}}{n_\lambda^1} =$$

$$\frac{\pi}{\hbar^2} \sum_{\lambda'\lambda''} |\Psi_{-\lambda\lambda'\lambda''}|^2 \Big[(1 + n_{\lambda'} + n_{\lambda''})\delta(\omega_\lambda - \omega_{\lambda'} - \omega_{\lambda''}) \tag{2.27}$$

$$+ (n_{\lambda'} - n_{\lambda''})\Big(\delta(\omega_\lambda + \omega_{\lambda'} - \omega_{\lambda''}) - \delta(\omega_\lambda - \omega_{\lambda'} + \omega_{\lambda''})\Big) \Big]$$

The RTA is thus a good approximation when phonon occupations n_λ are roughly constant in time, i.e., near equilibrium and in steady state, but is likely to fail if the system is far from equilibrium and varies strongly in time. Using the RTA, the LBTE Eq. (2.24) simplifies to

$$\frac{\partial n_\lambda^1}{\partial t} + \boldsymbol{v}_\lambda \cdot \nabla T \frac{\hbar\omega_\lambda}{k_B T^2} n_\lambda^0 (n_\lambda^0 + 1) = -\frac{n_\lambda^1}{\tau_\lambda}, \tag{2.28}$$

with the solution

$$n_\lambda^1(t) = -\tau_\lambda \boldsymbol{v}_\lambda \cdot \nabla T \frac{\hbar\omega_\lambda}{k_B T^2} n_\lambda^0 (n_\lambda^0 + 1) + \delta n_\lambda \exp(-t/\tau_\lambda), \tag{2.29}$$

where δn_λ is determined by the initial perturbation $n_\lambda^1(t = 0)$.

Once the LBTE is solved and the n_λ^1 are obtained, the thermal conductivity can be calculated from Fourier's law

$$J^\alpha = -\kappa^{\alpha\beta}\nabla_\beta T = \frac{1}{V} \sum_\lambda \hbar\omega_\lambda v_\lambda^\alpha n_\lambda, \tag{2.30}$$

where the rightmost expression describes the sum of individual mode energy fluxes. In equilibrium $n_\lambda = n_{-\lambda}$ (where $-\lambda = (-\boldsymbol{q})j$), and since $v_\lambda^\alpha = -v_{-\lambda}^\alpha$ and $\omega_\lambda = \omega_{-\lambda}$, the contribution to J^α from n_λ^0 cancels that from $n_{-\lambda}^0$. Therefore J^α can be simplified to

$$J^\alpha = \frac{1}{V} \sum_\lambda \hbar\omega_\lambda v_\lambda^\alpha n_\lambda^1. \tag{2.31}$$

Using the steady state LBTE solution under the RTA, the heat current becomes

$$J^\alpha = -\frac{1}{V} \sum_\lambda k_B \left(\frac{\hbar\omega_\lambda}{k_B T}\right)^2 n_\lambda^0 (n_\lambda^0 + 1)\tau_\lambda v_\lambda^\alpha v_\lambda^\beta \nabla_\beta T. \tag{2.32}$$

Identifying the specific heat of mode λ

$$c_\lambda = \frac{\partial E_\lambda}{\partial T} = \frac{\partial}{\partial T}\left(\hbar\omega_\lambda n_\lambda\right) = k_B \left(\frac{\hbar\omega_\lambda}{k_B T}\right)^2 n_\lambda^0(n_\lambda^0 + 1), \qquad (2.33)$$

J^α can be further simplified as

$$J^\alpha = -\frac{1}{V}\sum_\lambda c_\lambda \tau_\lambda v_\lambda^\alpha v_\lambda^\beta \nabla_\beta T. \qquad (2.34)$$

Finally, the thermal conductivity tensor is obtained by comparison with Fourier's law Eq. (2.30)

$$\kappa^{\alpha\beta} = \frac{1}{V}\sum_\lambda c_\lambda \tau_\lambda v_\lambda^\alpha v_\lambda^\beta. \qquad (2.35)$$

Hence, under these approximations, the thermal conductivity is determined by the relaxation times and group velocities of the phonon modes. Contributions to $\kappa^{\alpha\beta}$ are dominated by modes with high group velocities, i.e., predominantly acoustic modes.

2.4 Mode projection

Phonon mode occupation numbers $n_\lambda(t)$ can be acquired during MD simulations by projecting real state space coordinates $\boldsymbol{u}_{n\mu}(t)$ and $\boldsymbol{p}_{n\mu}(t)$ onto phonon mode coordinates $Q_\lambda(t)$ and $\Pi_\lambda(t)$ using some appropriate choice of basis functions $\boldsymbol{A}_{\mu j}$. The basis can be defined by diagonalizing the dynamical matrix $D_{\mu\mu'}^{\alpha\alpha'}(\boldsymbol{q})$, but a full diagonalization for a large system can be computationally prohibitive. Instead, one option is to calculate $D_{\mu\mu'}^{\alpha\alpha'}(\boldsymbol{q})$ only for the $\boldsymbol{q}$ which are to be studied. This would result in an incomplete set of basis functions, and is only a problem if the phonon coordinates need to be transformed back into real-space coordinates.

At finite temperatures, the presence of higher-order force contributions change the average forces between pairs of atoms from those given by the $0\,\text{K}$ second-order force constants. As a result, the optimal definition of basis functions would require constructing and diagonalizing $D_{\mu\mu'}^{\alpha\alpha'}(\boldsymbol{q})$ from the renormalized second-order force constants. Alternatively, the $0\,\text{K}$ eigenvectors can be paired with renormalized phonon mode frequencies $\omega_\lambda(T)$ to accurately describe the system if higher-order effects are small enough to be considered perturbations. The following section describes how to use phonon coordinates acquired from MD simulations to calculate the renormalized frequencies as well as the phonon mode lifetimes used to describe the LTC in section 2.3.

Some unexpected problems arise when trying to set phonon coordinates to specific values and transforming them to atomic coordinates. Since this is precisely what need to be done to create initial states for mode pumping experiments, the final section in this chapter describes the arising problems and how to handle them.

2.4.1 Time evolution of phonon coordinates

If the system used in a MD simulation is purely harmonic, then the equation for the mode displacement of some mode λ is described by

$$\frac{\partial^2}{\partial t^2} Q_\lambda + \omega_\lambda^2 Q_\lambda = 0, \tag{2.36}$$

and the resulting $Q_\lambda(t)$ and $\Pi_\lambda(t)$ will be sinusoidal with some amplitude B and phase φ,

$$\begin{aligned} Q_\lambda(t) &= B\sin(\omega_\lambda t + \varphi) \\ \Pi_\lambda(t) &= \omega_\lambda B\cos(\omega_\lambda t + \varphi). \end{aligned} \tag{2.37}$$

The potential and kinetic energies of mode λ can be identified in Eq. (2.10) and are simply $U_\lambda = \frac{1}{2}\omega_\lambda^2|Q_\lambda(t)|^2$ and $K_\lambda = \frac{1}{2}|\Pi_\lambda(t)|^2$, respectively. The total energy of the mode can therefore be expressed in terms of the mode amplitude as $E_\lambda = \omega_\lambda^2|B|^2$. In equilibrium at temperature T, the system would have an energy of $\frac{1}{2}k_B T$ per degree of freedom, according to the equipartition theorem. Since each phonon mode represents two degrees of freedom, the average energy per mode is $\langle E_\lambda \rangle = k_B T$ in equilibrium. This means the average mode amplitude at temperature T is

$$\langle |B| \rangle (T) = \frac{\sqrt{k_B T}}{\omega_\lambda}, \tag{2.38}$$

which gives a convenient measure for B. Instead of directly stating the value of B, which has dimensions $(\text{mass})^{\frac{1}{2}} \cdot (\text{length})$, it can be stated in terms of the temperature at which B would be the mean amplitude.

2.4.2 Damped harmonic oscillator

In the presence of anharmonicities, Eq. (2.36) can be adjusted by including a damping term $\Gamma(T)\frac{\partial}{\partial t}Q$ describing relaxation and a force term $f(t)$ describing thermal fluctuations,

$$\frac{\partial^2}{\partial t^2} Q_\lambda + \Gamma(T)\frac{\partial}{\partial t} Q_\lambda + \omega_\lambda(T)^2 Q_\lambda = f(t). \tag{2.39}$$

This is a Langevin equation, modeling Q_λ and $f(t)$ as random variables, where $f(t)$ is assumed to behave as white noise, meaning $\langle f(t) \rangle_t = 0$ and $\langle f(t)f^*(t + \Delta t) \rangle_t = F\delta(\Delta t)$. Furthermore, the oscillation frequency and damping factor are explicitly written to be temperature dependent to account for any thermal softening and hardening due to the anharmonic force contributions. For simplicity, however, we drop the temperature dependence in the following.

Solving Eq. (2.39) for $Q_\lambda(t)$ directly would be troublesome and not very useful due to the inclusion of the random force. Instead, the equation can be used to model the autocorrelation function of $\Pi_\lambda = \frac{\partial}{\partial t}Q_\lambda$. Fourier transforming Eq. (2.39) gives

$$\left[-\omega^2 + i\Gamma\omega + \omega_\lambda^2 \right] \hat{Q}_\lambda(\omega) = \hat{f}(\omega), \tag{2.40}$$

where

$$\hat{u}(\omega) = \mathcal{F}[u(t)](\omega) = \int_{-\infty}^{\infty} u(t)e^{-i\omega t}\, dt$$

is the Fourier transform of $u(t)$, and $\mathcal{F}[\frac{\partial^n}{\partial t^n}u] = (i\omega)^n\mathcal{F}[u]$ has been used. According to the Wiener-Khinchin theorem, the autocorrelation function of a function $u(t)$

$$C_u(\Delta t) = \langle u(t)u^*(t + \Delta t)\rangle_t$$

obeys

$$\hat{C}_u(\omega) = |\hat{u}(\omega)|^2. \tag{2.41}$$

In other words, the autocorrelation function is given by the inverse Fourier transform of the power spectrum. Taking the absolute value squared of Eq. (2.40), using $\mathcal{F}[\delta(\Delta t)] = 1$, and rearranging gives the power spectrum [17]

$$\hat{C}_{Q_\lambda}(\omega) = |\hat{Q}_\lambda(\omega)|^2 = \frac{F}{(\omega^2 - \omega_\lambda^2)^2 + \Gamma^2\omega^2}. \tag{2.42}$$

Inverse Fourier transforming this expression for $\omega_\lambda > \Gamma/2$ gives

$$C_{Q_\lambda}(\Delta t) = \frac{F}{2\Gamma\omega_\lambda}e^{-\frac{1}{2}\Gamma|\Delta t|}\left[\cos(\omega_e\Delta t) + \frac{\Gamma}{2\omega_e}\sin(\omega_e|\Delta t|)\right], \tag{2.43}$$

where $\omega_e = \sqrt{\omega_\lambda^2 - \frac{1}{4}\Gamma^2}$. At this point the relaxation time can be identified from the exponent as $\tau_\lambda = \frac{2}{\Gamma}$. The autocorrelation function for Π_λ can be derived from C_{Q_λ} by noting that

$$\hat{C}_{\Pi_\lambda} = |\Pi_\lambda|^2 = |-i\omega Q_\lambda|^2 = \omega^2|Q_\lambda|^2 = \omega^2\hat{C}_{Q_\lambda} = \mathcal{F}\left[-\frac{\partial^2}{\partial\Delta t^2}C_{Q_\lambda}\right],$$

meaning

$$C_{\Pi_\lambda}(\Delta t) = -\frac{\partial^2}{\partial\Delta t^2}C_{Q_\lambda}(\Delta t).$$

Taking the second derivative of Eq. (2.43) thus yields

$$C_{\Pi_\lambda}(\Delta t) = \frac{\omega_\lambda}{2\Gamma}Fe^{-\frac{1}{2}\Gamma|\Delta t|}\left[\cos(\omega_e\Delta t) + \frac{\Gamma}{2\omega_e}\sin(\omega_e|\Delta t|)\right].$$

Since the average kinetic energy of mode λ is $K_\lambda = \frac{1}{2}|\Pi_\lambda|^2 = \frac{1}{2}C_{\Pi_\lambda}(0)$ and the equipartition theorem states $K_\lambda = \frac{1}{2}k_BT$, in equilibrium the force factor F must be

$$F = \frac{2\Gamma k_BT}{\omega_\lambda(T)}$$

and

$$C_{\Pi_\lambda}(\Delta t) = k_BTe^{-\frac{1}{2}\Gamma|\Delta t|}\left[\cos(\omega_e(T)\Delta t) + \frac{\Gamma}{2\omega_e(T)}\sin(\omega_e(T)|\Delta t|)\right]. \tag{2.44}$$

Next, the phonons are assumed to oscillate much faster than they relax, so that $\Gamma \ll \omega_\lambda(T)$. As a result $\omega_e(T) \approx \omega_\lambda(T)$ and $\frac{\Gamma}{2\omega_e(T)} \approx 0$. The momentum autocorrelation function is simplified to

$$C_{\Pi_\lambda}(\Delta t) \approx k_BTe^{-\frac{1}{2}\Gamma|\Delta t|}\cos(\omega_\lambda(T)\Delta t), \tag{2.45}$$

13

and its power spectrum to

$$\hat{C}_{\Pi_\lambda}(\omega) \approx \frac{(\Gamma/2)k_B T}{(\omega - \omega_\lambda(T))^2 + (\Gamma/2)^2}. \tag{2.46}$$

Finally, expressing the power spectrum in terms of the relaxation time gives a Lorentzian function

$$\hat{C}_{\Pi_\lambda}(\omega) = \frac{\tau_\lambda(T)k_B T}{1 + \tau_\lambda(T)^2(\omega - \omega_\lambda(T))^2}. \tag{2.47}$$

Projecting a MD trajectory onto phonon mode coordinates, calculating the power spectrum of Π_λ, and fitting a Lorentzian function to it is thus a way to calculate the renormalized frequencies $\omega_\lambda(T)$ and relaxation times $\tau_\lambda(T)$.

2.4.3 Mode pumping

When projecting atomic displacements $u_{n\mu}^\alpha$ and momenta $p_{n\mu}^\alpha$ onto normal coordinates $Q_j(\boldsymbol{q})$ and $\Pi_j(\boldsymbol{q})$, the process is straightforward, since Eq. (2.8) can be calculated directly. Some care must, however, be taken when the aim is to choose $u_{n\mu}^\alpha$ and $p_{n\mu}^\alpha$ to attain a set of $Q_j(\boldsymbol{q})$ and $\Pi_j(\boldsymbol{q})$. This is the case in mode pumping simulations, where an equilibrated system is altered such that a specific mode $(\boldsymbol{q}, j)$ acquires a desired energy $\hbar\omega_j(\boldsymbol{q})(n_{\boldsymbol{q}j} + \frac{1}{2}) = \frac{1}{2}|\Pi_j(\boldsymbol{q})|^2 + \frac{1}{2}\omega_j(\boldsymbol{q})^2|Q_j(\boldsymbol{q})|^2$. The situation is complicated by the fact that phonon eigenvectors $A_{\mu j}^\alpha$ can have an arbitrary complex phase which factors into $Q_j(\boldsymbol{q})$ and $\Pi_j(\boldsymbol{q})$. If, for a given $A_{\mu j}^\alpha$, $Q_j(\boldsymbol{q})$ and $\Pi_j(\boldsymbol{q})$ are set to specific amplitudes consistent with some mode occupation $n_{\boldsymbol{q}j}$ but with arbitrary phases, then the resulting computed atomic displacements and momenta are likely to be complex. What follows is an investigation of the optimal choice of complex phase for $Q_j(\boldsymbol{q})$ to obtain a purely real set of displacements $u_{n\mu}^\alpha$. For simplicity, consider a system where only a single mode $(\boldsymbol{q}, j)$ is occupied, $Q'_j(\boldsymbol{q}') \propto \delta_{\boldsymbol{q}', \pm\boldsymbol{q}}\delta_{j',j}$. The displacements $u_{n\mu}^\alpha$ can readily be expressed in terms of $Q_j(\boldsymbol{q})$ as

$$u_{n\mu}^\alpha = \frac{c}{\sqrt{Nm_\mu}} Re\left[A_{\mu j}^\alpha(\boldsymbol{q})e^{i\boldsymbol{q}\cdot\boldsymbol{R}_n^0}Q_j(\boldsymbol{q})\right], \tag{2.48}$$

where $c = 1$ if $\boldsymbol{q}$ and $-\boldsymbol{q}$ are separated by a reciprocal lattice vector and $c = 2$ otherwise. In the former case $\boldsymbol{q}$ and $-\boldsymbol{q}$ are equivalent when folded into the first Brillouin zone (BZ), while in the latter case, the factor of two appears because both $Q_j(\boldsymbol{q})$ and $Q_j(-\boldsymbol{q})$ appear in the sum and their terms are complex conjugates. For brevity, the notation is simplified,

$$\begin{aligned} u_{n\mu}^\alpha &= \boldsymbol{u}, \\ \frac{1}{\sqrt{Nm_\mu}}A_{\mu j}^\alpha(\boldsymbol{q})e^{i\boldsymbol{q}\cdot\boldsymbol{R}_n^0} &= \boldsymbol{A} = \boldsymbol{A}_r + i\boldsymbol{A}_i \\ Q_j(\boldsymbol{q}) &= Q_r + iQ_i, \end{aligned} \tag{2.49}$$

whence

$$\boldsymbol{u} = c\,Re[Q_r\boldsymbol{A}_r - Q_i\boldsymbol{A}_i + i(Q_r\boldsymbol{A}_i + Q_i\boldsymbol{A}_r)]. \tag{2.50}$$

To pump the mode $\boldsymbol{q}j$, a complex phase ϕ needs to be chosen, where $Q = |Q|e^{i\phi}$, such that the real part in Eq. (2.50) is maximized independent of the amplitude $|Q|$. The quantity to maximize is

$$
\begin{aligned}
|Q_r \boldsymbol{A}_r - Q_i \boldsymbol{A}_i|^2 / |Q|^2 &= |\boldsymbol{A}_r \cos\varphi - \boldsymbol{A}_i \sin\varphi|^2 \\
&= |\boldsymbol{A}_r|^2 \cos^2\varphi + |\boldsymbol{A}_i|^2 \sin^2\varphi - 2\boldsymbol{A}_r \cdot \boldsymbol{A}_i \cos\varphi \sin\varphi \\
&= \frac{1}{2}|\boldsymbol{A}|^2 + \frac{1}{2}\left(|\boldsymbol{A}_r|^2 - |\boldsymbol{A}_i|^2\right)\cos 2\varphi - \boldsymbol{A}_r \cdot \boldsymbol{A}_i \sin 2\varphi .
\end{aligned}
\tag{2.51}
$$

The first term is constant and can be dropped. The remaining terms can be rewritten by using the trigonometric relation

$$
a\cos\theta + b\sin\theta = \sqrt{a^2 + b^2}\cos(\theta - \psi), \quad \text{where } \cos\psi = \frac{a}{\sqrt{a^2 + b^2}}.
\tag{2.52}
$$

The expression to maximize becomes

$$
\sqrt{\frac{1}{4}\left(|\boldsymbol{A}_r|^2 - |\boldsymbol{A}_i|^2\right)^2 + \left(\boldsymbol{A}_r \cdot \boldsymbol{A}_i\right)^2}\cos(2\varphi - \psi), \quad \text{where}
$$
$$
\cos\psi = \frac{|\boldsymbol{A}_r|^2 - |\boldsymbol{A}_i|^2}{\sqrt{\left(|\boldsymbol{A}_r|^2 - |\boldsymbol{A}_i|^2\right)^2 + 4\left(\boldsymbol{A}_r \cdot \boldsymbol{A}_i\right)^2}}.
\tag{2.53}
$$

Since $\cos\theta$ has its maximum at $\theta = 0$, the expression is maximized by $\varphi = \frac{\psi}{2}$. This solution can also be expressed as

$$
\cos 2\varphi = \cos\psi = \frac{|\boldsymbol{A}_r|^2 - |\boldsymbol{A}_i|^2}{\sqrt{\left(|\boldsymbol{A}_r|^2 - |\boldsymbol{A}_i|^2\right)^2 + 4\left(\boldsymbol{A}_r \cdot \boldsymbol{A}_i\right)^2}},
\tag{2.54}
$$

which gives computationally convenient access to the real and imaginary parts of Q through

$$
\begin{aligned}
\cos\varphi &= \pm\sqrt{\frac{1 + \cos 2\varphi}{2}} \\
\sin\varphi &= \pm\sqrt{\frac{1 - \cos 2\varphi}{2}},
\end{aligned}
\tag{2.55}
$$

where the choice of sign is arbitrary.

An issue remains regarding Eq. (2.54), though, which is what happens at the limits $|\boldsymbol{A}_r|^2 = |\boldsymbol{A}_i|^2$ and/or $\boldsymbol{A}_r \cdot \boldsymbol{A}_i = 0$. If either, but not both, quantity is zero then the result is straightforward. In case $|\boldsymbol{A}_r|^2 = |\boldsymbol{A}_i|^2$ and $\boldsymbol{A}_r \cdot \boldsymbol{A}_i \neq 0$, then Eq. (2.54) is simply zero. Similarly, if $|\boldsymbol{A}_r|^2 \neq |\boldsymbol{A}_i|^2$ and $\boldsymbol{A}_r \cdot \boldsymbol{A}_i = 0$, then the expression reduces to $\mathrm{sgn}(|\boldsymbol{A}_r|^2 - |\boldsymbol{A}_i|^2)$. If, however, both quantities are zero, then Eq. (2.54) is undefined, and its limit depends on how the two quantities approach zero. The explanation is given in the last line of Eq. (2.51), which in this case simplifies to

$$
|Q_r \boldsymbol{A}_r - Q_i \boldsymbol{A}_i|^2 = \frac{1}{2}|Q\boldsymbol{A}|^2 ,
\tag{2.56}
$$

i.e., the vector whose norm we want to maximize has constant norm. The choice of complex phase φ is thus completely arbitrary in this case.

The remaining obstacle is to determine when the case $|\boldsymbol{A}_r|^2 - |\boldsymbol{A}_i|^2 = \boldsymbol{A}_r \cdot \boldsymbol{A}_i = 0$ occurs. Consider

$$\boldsymbol{A} = \frac{1}{\sqrt{Nm_\mu}} A_{\mu j}^\alpha(\boldsymbol{q}) e^{i\boldsymbol{q} \cdot \boldsymbol{R}_n^0} \tag{2.57}$$

in the case of a monatomic linear chain of length N, with atomic weight $m_\mu = m$. The distance vector between two neighboring atoms is denoted $\boldsymbol{A}$. Fixing one atom in the chain to equilibrium position $\boldsymbol{R}_0^0 = 0$, the remaining equilibrium positions are described by $\boldsymbol{R}_n^0 = n\boldsymbol{A}$, $n = 0, \ldots, N - 1$. The single reciprocal lattice basis vector is denoted $\boldsymbol{b}$ and fulfills $\boldsymbol{A} \cdot \boldsymbol{b} = 2\pi$. Commensurate wave vectors can then be expressed as $\boldsymbol{q}_l = \frac{l}{N}\boldsymbol{b}$, where integers $l = -(N - 1)/2, \ldots, (N - 1/2)$ if N is odd and $l = -(N - 2)/2, \ldots, N/2$ if N is even. The vector under consideration can now be expressed as

$$A_k^\alpha(l) = \frac{1}{\sqrt{Nm}} A_0^\alpha(l) e^{i2\pi \frac{nl}{N}} \tag{2.58}$$

Two classes of wave vectors can be identified. Zero and BZ boundary points, $l = 0$ and $l = N/2$, cause the exponent $2\pi nl/N$ to be an integer multiple of π, meaning the phase factor $e^{i\boldsymbol{q}_l \cdot \boldsymbol{R}_n^0}$ becomes entirely real. If the eigenvector components $A_0^\alpha(l)$, corresponding to displacements of the first atom, are real, then the entire eigenvector is real. Similarly, if $A_0^\alpha(l)$ has a complex phase then the full eigenvector will have the same complex phase, and the preceding real part maximization can be used to find this complex phase. The other class consists of all the other wave vectors, and encompasses almost all l if N is not small. The real and imaginary parts of $\boldsymbol{A}$, assuming for simplicity $A_0^\alpha(l)$ is real, are

$$\begin{aligned}
A_{kr}^\alpha(l) &= \frac{1}{\sqrt{Nm}} A_0^\alpha(l) \cos\left(\frac{2\pi nl}{N}\right) \\
A_{ki}^\alpha(l) &= \frac{1}{\sqrt{Nm}} A_0^\alpha(l) \sin\left(\frac{2\pi nl}{N}\right).
\end{aligned} \tag{2.59}$$

Their magnitudes are

$$\begin{aligned}
|\boldsymbol{A}_r(l)|^2 &= \frac{1}{Nm} \sum_\alpha (A_0^\alpha(l))^2 \sum_{n=0}^{N-1} \cos^2\left(\frac{2\pi nl}{N}\right) \\
&= \frac{1}{2Nm} \sum_\alpha (A_0^\alpha(l))^2 \sum_{n=0}^{N-1} \left[1 + \cos\left(\frac{4\pi nl}{N}\right)\right] \\
&= \frac{1}{2m} \sum_\alpha (A_0^\alpha(l))^2
\end{aligned} \tag{2.60}$$

and

$$\begin{aligned}
|\boldsymbol{A}_i(l)|^2 &= \frac{1}{Nm} \sum_\alpha (A_0^\alpha(l))^2 \sum_{n=0}^{N-1} \sin^2\left(\frac{2\pi nl}{N}\right) \\
&= \frac{1}{2Nm} \sum_\alpha (A_0^\alpha(l))^2 \sum_{n=0}^{N-1} \left[1 - \cos\left(\frac{4\pi nl}{N}\right)\right] \\
&= \frac{1}{2m} \sum_\alpha (A_0^\alpha(l))^2,
\end{aligned} \tag{2.61}$$

where $\sum_{n=0}^{N-1} \cos(4\pi n l/N) = 0$ has been used. This equality holds for $0 < l < N/2$, and can be understood by considering the regular polygon described by $\exp(i4\pi n l/N)$ in the complex plane. This polygon has $d = N/(2\gcd(l,N))$ edges and by symmetry, the sum of its edge coordinates is zero. If $l = 0$ or $l = N/2$ then $d = 1$ and the sum is nonzero. The important result here is that, for the class of l under consideration, $|\boldsymbol{A}_r(l)|^2 = |\boldsymbol{A}_i(l)|^2$. For the other important quantity, a similar calculation yields

$$
\begin{aligned}
\boldsymbol{A}_r(l) \cdot \boldsymbol{A}_i(l) &= \frac{1}{Nm} \sum_\alpha (A_0^\alpha(l))^2 \sum_{n=0}^{N-1} \cos\left(\frac{2\pi n l}{N}\right) \sin\left(\frac{2\pi n l}{N}\right) \\
&= \frac{1}{2Nm} \sum_\alpha (A_0^\alpha(l))^2 \sum_{n=0}^{N-1} \sin\left(\frac{4\pi n l}{N}\right) = 0.
\end{aligned}
\tag{2.62}
$$

Hence, for wave vectors away from zero and the BZ boundary, the amplitude of the real part of $Q\boldsymbol{A}$ is constant, $|Q_r\boldsymbol{A}_r - Q_i\boldsymbol{A}_i|^2 = |Q\boldsymbol{A}|^2/2$. Furthermore, since the constant $c = 2$ when $\boldsymbol{q}$ and $-\boldsymbol{q}$ are not equivalent and this occurs exactly when $\boldsymbol{q}$ is away from zero and the BZ boundary, the norm of Eq. (2.50) is simply

$$
|\boldsymbol{u}|^2 = 2|Q\boldsymbol{A}|^2
\tag{2.63}
$$

for these wave vectors. For the zero and BZ boundary points, the result is the same but without the factor 2 when the phase of Q has been optimized.

3

Results

3.1 Overview

The posed problem was investigated by the use of large-scale MD simulations of stacks of graphene using graphical processing units (GPUs) via the GPUMD package [13] and its CALORINE Python interface [7]. Graphene was chosen since it is a prototype material for thin film stacks and is simple to model due to consisting entirely of a single element and having a simpler structure than, e.g., TMDs. In order to model stacks of rotated graphene sheets, some care is required. Two stacked layers with a *random* twist angle generally do not result in a fully periodic system, or at least not in a system with short enough period lengths. This is a problem for computational methods such as MD simulations, since crystals are most commonly modeled using periodic boundary conditions to avoid edge effects. In order to get around this problem, moiré lattices [18] were used.
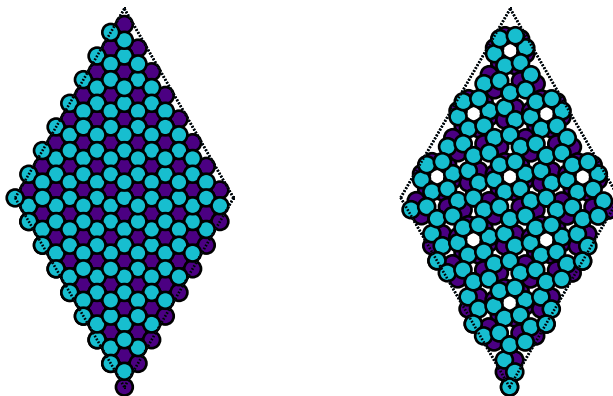

Figure 3.1: Comparison between regular graphite and a moiré lattice. The panels show two atomic layers of graphite (left) and the simplest moiré structure (right). All atoms are carbon, but for legibility the front layer atoms are shown in blue and the back layer atoms in purple. Not that the moiré lattice is periodic, even though it's layers are rotated ($\theta = 21.8°$) relative to each other.

Each such stacked structure is characterized by one twist angle, which is the relative rotation between the two layers in the conventional unit cell. As the unit cell is repeated in a supercell, the layers are thus stacked with alternating rotations.
All calculations were managed using PYTHON, and all atomic structures were represented and handled using ASE [21]. Throughout all simulations, the potential energy

was modeled using NEPs [14] trained on the results of DFT calculations. FCs were constructed by fitting FCPs to the NEPs using the HIPHIVE package [12], in conjunction with some features of the PHONOPY package [30]. The FCs were then used to construct dynamical matrices, which in turn were diagonalized to obtain phonon eigenvectors and harmonic frequencies.

To obtain equilibrium phonon lifetimes and anharmonic frequencies, MD simulations were performed where an initial equilibration period in the NVT ensemble using the Langevin thermostat was followed by a production run in the NVE ensemble. All MD simulations were performed on GPUs on high-performance computing clusters using GPUMD. While this allows for simulations of systems on the order of 10^5 to 10^7 atoms [13], such sizes are not necessary for the task at hand. Rather priority was given to performing a variety of simulations and repeating them to acquire good statistics. Hence, system sizes between 10^3 and 10^4 atoms were used. This was small enough to enable efficient calculations and data management, while still being large enough to represent a thermodynamic ensemble. Furthermore, it was large enough to resolve the BZ well enough to include the modes most relevant for scattering with the modes of interest. Too small simulation cells would not be able to account for prominent relaxation paths, and lifetimes would thus appear longer. All MD simulations were performed with a time step of 1 fs.

Each time step in the resulting trajectories was projected onto phonon coordinates to obtain phonon mode displacements $Q_\lambda(t)$ and momenta $P_\lambda(t)$ as functions of time. Modeling the momenta as amplitudes of independent damped harmonic oscillators then enabled the extraction of equilibrium lifetimes and renormalized frequencies, differing from the harmonic eigenfrequencies due to the presence of anharmonic force contributions.

Next, phonon mode relaxation simulations were performed by projecting the positions and velocities of thermally equilibrated structures onto $Q_\lambda(0)$ and $P_\lambda(0)$. For the pumped mode, $Q_\lambda(0)$ was then set to zero, while $P_\lambda(0)$ was set to a value consistent with the desired pumping temperature. After projecting the modified phonon displacements and momenta back onto atomic positions and velocities, the resulting structures were used as the initial states in NVE ensemble MD simulations. The resulting trajectories were once again projected onto $Q_\lambda(t)$ and $P_\lambda(t)$ to obtain phonon mode energies as a function of time, and the energy of the pumped mode was analyzed to find relaxation paths and non-equilibrium lifetimes.

3.2 Energy Landscape

A NEP was trained on data from DFT calculations using the vdW-DF-CX functional [2, 20, 10] to use as the model for the potential energy U in Eq. (2.1) for all calculations [11]. The validity of the trained NEP is indicated in Figs. 3.2 and 3.3, where potential energies predicted by the NEP are compared to those from DFT calculations. Figure 3.2 shows the binding energy curve, i.e., the potential energy as a function of inter-layer distance. In Fig. 3.3, slip surface plots are shown, illustrating how the potential energy varies as neighboring atomic layers are displaced relative to each other along two directions (Fig. 3.3a) and along a line crossing both the minimum and maximum energy (Fig. 3.3b).
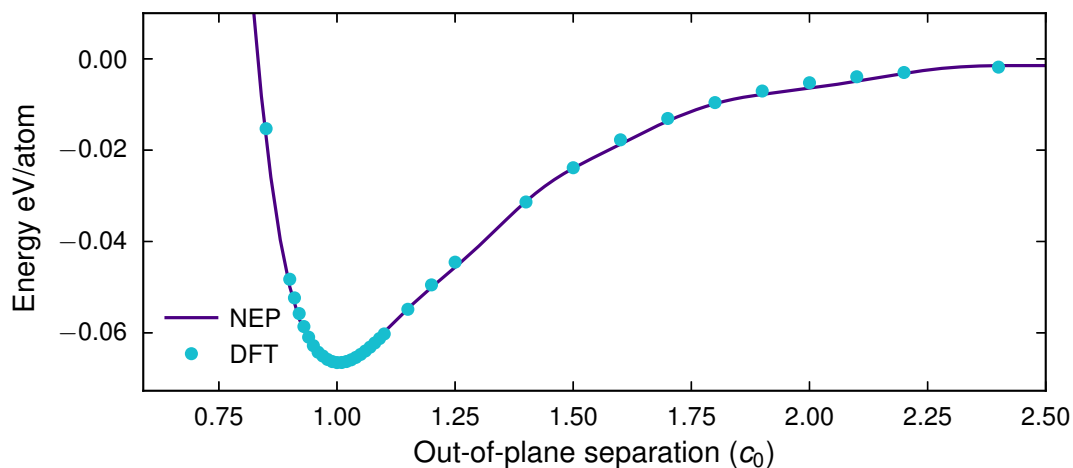
Figure 3.2: Binding energy. The potential energy from DFT (light blue dots) and the NEP (solid purple line) is shown as a function of the distance between atomic layers in graphite.

In order to construct the harmonic FCs in Eqs. (2.2) and (2.3), the structures were first relaxed to minima in U using the ASE implementation of the Broyden-Fletcher-Goldfarb-Shanno optimization algorithm. For the most stable structure, regular graphite, the symmetry was also kept fixed by the use of a `FixSymmetry` [31] constraint. At $0\,\text{K}$, a `UnitCellFilter` [28] was additionally used to enable relaxation of lattice parameters. At nonzero temperatures, the lattice parameters were instead determined from MD simulations in the NPT ensemble. A model was fitted [11] for in-plane and out-of-plane lattice constants $a(T)$ and $c(T, \theta)$, respectively, as a function of temperature T and twist angle θ.

$$a(T) = a_0(1 + \lambda_a T)$$
$$c(T, \theta) = c_{\text{AA}}(T) + (c_{\text{AB}}(T) - c_{\text{AA}}(T))e^{-k(T)\theta}, \tag{3.1}$$

where

$$c_{\text{X}}(T) = c_{\text{X},0}(1 + \lambda_{\text{X}}T), \ \text{X} \in \{\text{AA}, \text{AB}\}$$
$$k(T) = k_0(1 - \lambda_k T).$$

A plot of $c(T, \theta)$ is shown in Figure 3.4 and the model parameters are shown in Table 3.1. Here, θ is the twist angle in degrees between the two graphene layers in the conventional unit cell. The case $\theta = 60°$ corresponds to AA stacking, meaning atoms in the two layers are vertically aligned, while $\theta = 0°$ corresponds to AB stacking, where atoms in one layer are aligned with the gaps between atoms in the other layer.
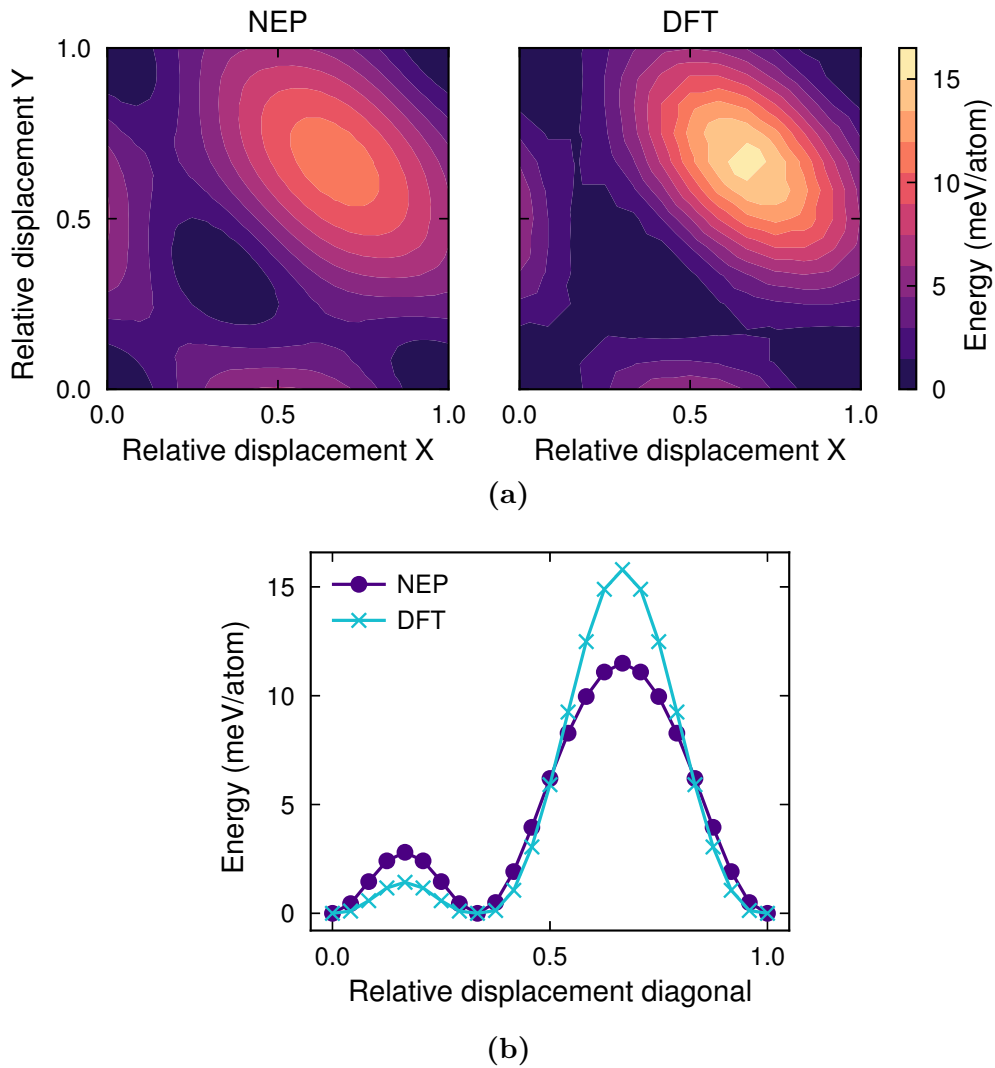
(a)

(b)

Figure 3.3: Slip surface. The potential energy from DFT and the NEP is shown as a function of the in-plane displacement of one layer relative to the relaxed structure, i.e., AB-stacking at $X = Y = 0$. Displacements in X and Y are given in coordinates relative to the primitive cell and due to the periodic boundary conditions, the slip surface is periodic in X and Y with period 1. (a) Potential energy as a function of relative displacement in X and Y from the NEP (left) and from DFT (right). (b) Potential energy as a function of the displacement along the diagonal $X = Y$ from the NEP (solid purple line with circles) and from DFT (solid light blue line with crosses).
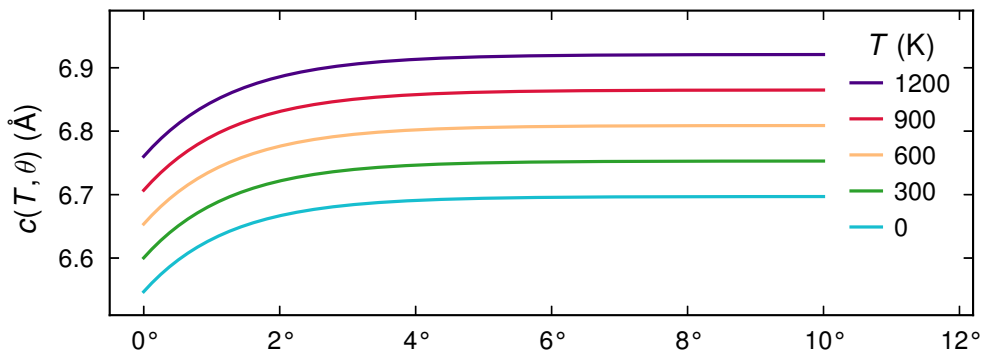
Figure 3.4: Out-of-plane lattice constant $c(T, \theta)$ in Eq. (3.1) for a variety of twist angles and temperatures. $\theta = 0°$ corresponds to AB stacked graphite, while $\theta = 60°$ corresponds to AA stacking.

Table 3.1: Graphene moiré structure thermal expansion parameters.

$a_0 = 2.4673\,\text{Å}$	$\lambda_a = 1.3944 \times 10^{-6}\,\text{K}^{-1}$	$c_{\text{AB},0} = 6.547\,\text{Å}$	$\lambda_{\text{AB}} = 27.133 \times 10^{-6}\,\text{K}^{-1}$
$k_0 = 0.799$	$\lambda_k = 40.021 \times 10^{-6}\,\text{K}^{-1}$	$c_{\text{AA},0} = 6.697\,\text{Å}$	$\lambda_{\text{AA}} = 27.857 \times 10^{-6}\,\text{K}^{-1}$

3.3 Harmonic Phonons

The relaxed primitive structures were then used with HIPHIVE and PHONOPY to train FCPs, which in turn were used to extract FCs for supercells. In order to train a FCP, an array of input structures along with their atomic forces as returned by the NEP was generated. Such input structures are often generated by randomly rattling the relaxed supercells but in order to improve the quality of the FCP and FCs, a few extra steps were taken to generate physically probable atomic displacements.

First, the primitive structure was repeated in every direction until no atom was closer to a periodic image of itself than the distance of the highest NEP cutoff (8.0 Å). In other words, the supercell was made large enough that the model never needs to evaluate the interaction of an atom with its periodic image. PHONOPY was used to construct an initial set of FCs, which is a relatively fast operation but results in FCs that lack permutation symmetries. To improve the FCs, the `generate_phonon_rattled_structures` function of HIPHIVE was employed next to generate a set of physically probable training structures. This was done by constructing phonon modes based on the PHONOPY FCs, and then displacing atomic positions according to the phonon modes with amplitudes randomly sampled from a thermal distribution at 5 K. This temperature was selected since it was considered low enough that thermal mode softening would essentially be non-existent, and the resulting structures could still be considered perturbations of the relaxed reference structure. Indeed, the average atomic displacement was below 0.05 Å, which can be compared to the interatomic distance between nearest neighbors of between
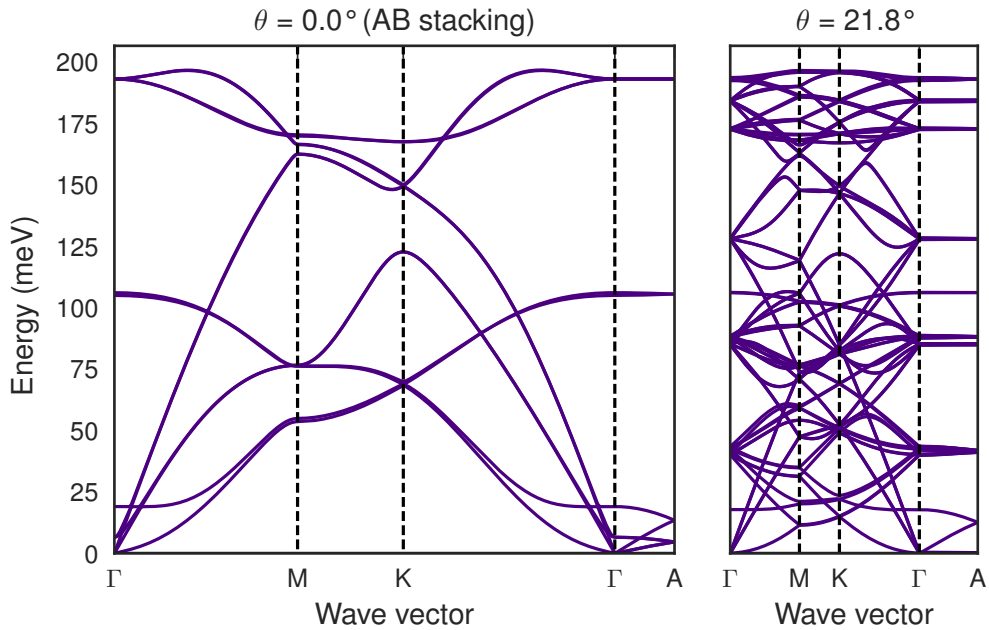
Figure 3.5: Harmonic phonon dispersion along the path $\Gamma MK\Gamma A$. The panel on the left shows the dispersion for AB-stacked graphite, while the panel on the right shows the dispersion for the simplest moiré structure.

2.8 Å and 3.7 Å. This set of training structures was then used to train the final FCP, simultaneously enforcing translation and permutation symmetries in the later extracted FCs.

The number of training structures in the final step was chosen to be at least five, such that the number of force components present in total in the training set was at least ten times the number of degrees of freedom in the HIPHIVE cluster space generated for the primitive structure. The cluster space was in turn generated using an interaction cutoff of 6.0 Å and a `symprec`, the tolerance for numerical deviations from exact spatial symmetry related quantities, of 1.0×10^{-3}.

Finally, PHONOPY was used to calculate harmonic dispersions from the FCs. Figure 3.5 shows the resulting band structure at $T = 0$ K for AB stacked graphite ($\theta = 0°$) and the simplest moiré structure ($\theta = 21.8°$).

Since the out-of-plane modes are of particular interest, Figure 3.6 shows the acoustic bands between Γ and A for graphite and the five simplest moiré structures. As the twist angle decreases and the unitcell increases in size, more optical bands appear. The figure illustrates that some of the added optical mode lie quite close to the longitudinal acoustic (LA) band at small twist angles. Note that the lowest band is negative for $\theta = 6.0°$, indicating an unsuccessful structure relaxation, but that the qualitative picture for the other bands is still useful.

From the dispersions, phonon frequencies and group velocities were extracted between Γ ($\boldsymbol{q} = [0, 0, 0]$) and A ($\boldsymbol{q} = [0, 0, 1/2]$, where the last coordinate is the out-of-plane direction), both of which are shown for the LA and transverse acoustic (TA) modes at $T = 0$ K in Figure 3.7. Frequencies were extracted in the A point, and group velocities were extracted near Γ.

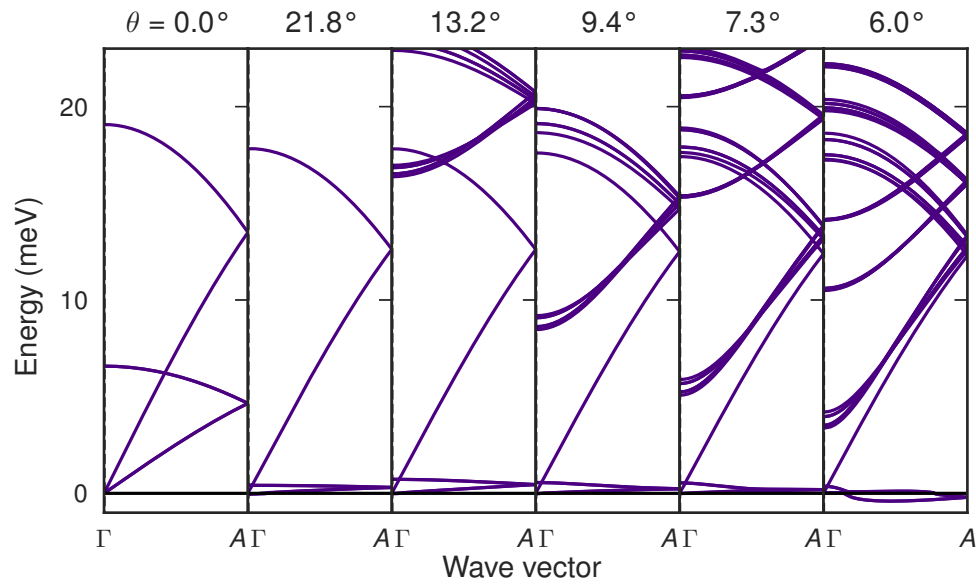**Figure 3.6:** Harmonic phonon dispersion between Γ and A, zoomed in on the acoustic modes and nearby optical modes.
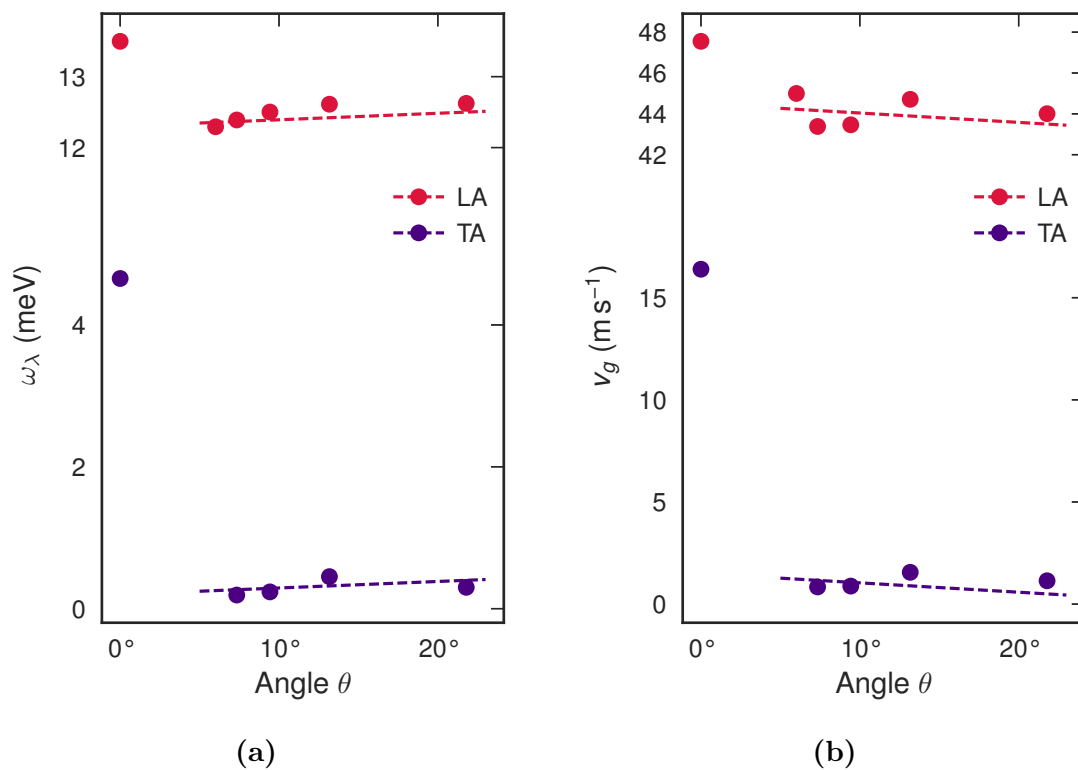

Figure 3.7: (a) Frequencies at the A-point and (b) group velocities at Γ in the direction of A as a function of twist angle. Frequencies and group velocities are shown in purple for the TA mode and red for the and LA mode. The dashed lines are guides to the eye.

In Figure 3.7, it is clear that increasing the twist angle above $\theta \approx 8°$ has little effect on the frequencies and group velocities. Smaller angles, on the other hand, are likely to show a stronger angle dependence. Unfortunately, smaller angle Moiré structures require larger unit cells, which becomes computationally prohibitive and is why Fig. 3.7 contains one more point for the LA mode than for the TA mode. The size of the $\theta = 6.0°$ structure caused small inaccuracies in relaxation and force constant determination, which resulted in the computed TA band being imaginary. Since the LA band is further from zero, it's determination is more robust against such inaccuracies, which is why it is still included in the figure.

3.4 Equilibrium Molecular Dynamics

For AB stacked graphite at $T = 300\,\mathrm{K}$, $400\,\mathrm{K}$, several equilibrium MD runs were performed. These runs consisted of an equilibration period of $200\,\mathrm{ps}$ in the NVT ensemble at the desired temperature, with a Langevin thermostat and a coupling factor $\gamma \Delta t = 100$, see Eq. (2.21). The equilibration period was followed by a production period of $1\,\mathrm{ns}$ in the NVE ensemble, where atomic positions, velocities and forces were stored every $20\,\mathrm{fs}$, resulting in trajectories of snapshots of said quantities. A supercell consisting of a $12 \times 12 \times 8$ repeated graphite unitcell (4608 atoms in total) was used in all simulations described in the following. The outputs were then used in two ways.

Firstly, a total of 20 snapshots evenly spaced in time were extracted from two separate MD runs, to be used as samples of the initial structure in thermal equilibrium. For $T = 400\,\mathrm{K}$, 20 snapshots additional snapshots were extracted from two simulations using a $12 \times 12 \times 16$ supercell (9216 atoms in total). The time difference between snapshots of $100\,\mathrm{ps}$ was chosen such that the samples can be considered uncorrelated.

Secondly, the velocities of all snapshots from three separate runs were projected onto phonon modes along a standard BZ path, giving a collection of phonon momenta time series. For each phonon mode, the momentum autocorrelation function was then modeled as a damped harmonic oscillator as described in section 2.4.2. Each run was split into four $250\,\mathrm{ps}$ time series individually used to calculate the mode momentum power spectra, resulting in a total of 12 power spectrum samples per temperature. The `curve_fit` function of SciPy was used to fit Eq. (2.47) to the sample means, with the sample standard deviations representing data uncertainties. In this way, the renormalized frequencies $\omega_\lambda(T)$ and relaxation times $\tau_\lambda(T)$ were obtained.

Since the sampling period was only $20\,\mathrm{fs}$, corresponding to a sampling frequency of $50\,\mathrm{THz}$, phonons bands with frequencies above the Nyquist frequency of $25\,\mathrm{THz}$ were analyzed through undersampling. If the harmonic frequency ω_λ of a band was above the Nyquist frequency $\omega_{\mathrm{Nyquist}}$, then the attained power spectrum at frequencies below $\omega_{\mathrm{Nyquist}}$ was assumed to be an alias of the power spectrum at frequencies $N\omega_{\mathrm{Nyquist}} < \omega < (N+1)\omega_{\mathrm{Nyquist}}$, where $N = \lfloor \omega_\lambda/\omega_{\mathrm{Nyquist}} \rfloor$. This assumption is usually problematic when the power spectrum is nonzero near the frequency interval borders, since in that case the aliasing distorts the power spectrum. These cases, however, were rare, and only happened for bands for which the renormalized fre-

quency was the primarily desired quantity. Hence, the distortion was not an issue, fitting the Lorentzian function still worked as a peak finding method, albeit the extracted lifetime was likely erroneous in those cases. The renormalized frequencies at 400 K are shown along with the harmonic dispersion at the same temperature in Fig. 3.8.
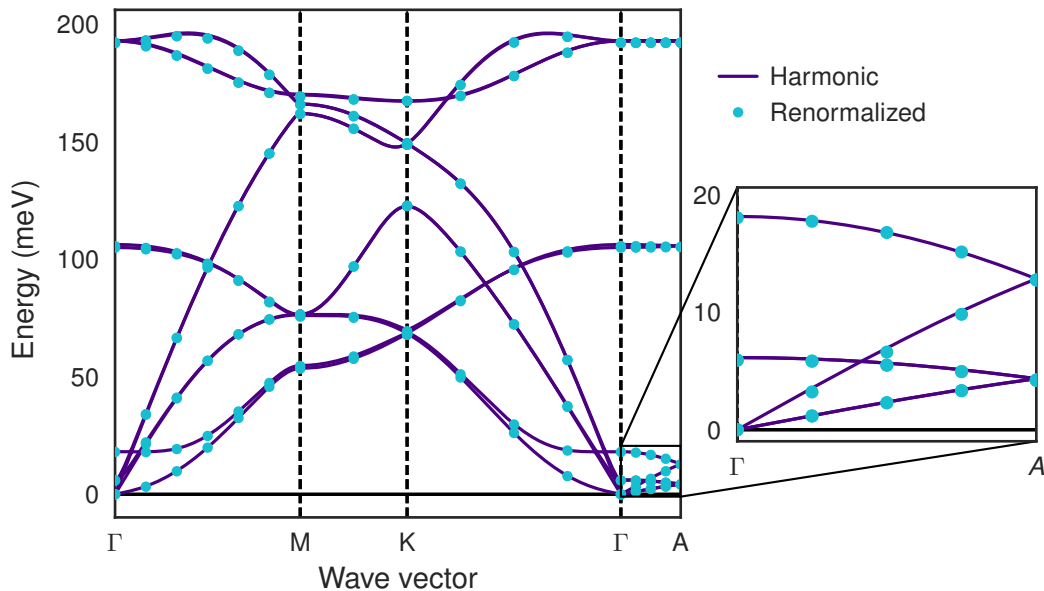

Figure 3.8: Phonon dispersion for AB-stacked graphite at 400 K. The solid purple line shows the harmonic frequencies of the relaxed structure, calculated as for the $T = 0$ K case, but using a structure with lattice constants thermally expanded at $T = 400$ K. The turquoise circles show renormalized frequencies extracted through fitting of damped harmonic oscillators.

Figure 3.8 shows that the renormalized frequencies are very close to the ones derived via the dynamical matrix with thermally expanded lattice constants. This means that most of the thermal mode softening or hardening can be accounted for by thermal expansion at these temperatures. It also indicates that the harmonic approximation works quite well for graphite at these temperatures, since anharmonic force contributions are not large enough to significantly disturb the harmonic picture.

3.5 Non-equilibrium Molecular dynamics

For the next series of runs, two phonon modes of particular interest were selected, a transverse optical (TO) mode at the Γ-point and a LA mode halfway between the Γ and A-points. For both selected phonon modes, and for both background temperatures, each of the 20 uncorrelated equilibrium $12 \times 12 \times 8$-supercell graphite snapshots was prepared in the following way. The displacement and momentum of the selected phonon mode was first set to zero in the snapshot structure by adjusting atomic positions and velocities via inverse phonon mode projection. Then, a series

of phonon pumped structures was prepared by setting the phonon momentum to a collection of amplitudes corresponding to the average kinetic energies at certain temperatures, $T_{\text{pump}} = 1250\,\text{K},\ 2500\,\text{K},\ 5000\,\text{K},\ 10\,000\,\text{K}$ and $20\,000\,\text{K}$.

Each of these TO-pumped (LA-pumped) structures was then used as the initial state in a 200 ps (20 ps) MD run in the NVE ensemble, where atomic positions and velocities were stored every 20 ps (2 ps). For every one of the 20 resulting trajectories, the atomic positions were projected onto phonon displacements and momenta, which were in turn used to calculate the kinetic, potential, and total energies of phonon modes. The energies from the 20 runs were finally used to calculate the energy mean and variance for the pumped mode. For the Γ-TO mode, the mean and variance were also calculated for the sum of the pumped mode energy with the energy of the other, degenerate, TO mode.

The same preparation as described above was done for the 20 $12 \times 12 \times 16$-supercell snapshots, but only for the LA mode at $T = 400\,\text{K}$ and $T_{\text{pump}} = 20\,000\,\text{K}$. These structures, along with the corresponding 20 $12 \times 12 \times 8$-supercell structures, were then used as initial states in MD simulations spanning 200 ps, where atomic coordinates were stored every 10 ps. Finally, the phonon energies were calculated as described for the previous runs.

3.5.1 Bayesian modeling

For all but the 200 ps LA pumping runs, the time series of the total energy of the pumped mode was then fitted to a decaying exponential function to extract the non-equilibrium lifetime. It should be noted that an exponential fit is a rather coarse approximation to the complex behavior observed in the data (see Figure 3.9). Firstly, the energy and time units were standardized to prevent numerical errors. Time was scaled relative to one picosecond, with time steps t_n ranging from $t_1 = 0.02\,(0.002)$ to $t_{10\,000} = 200\,(20)$ for the TO (LA) mode. The first time step was offset from zero because the initial states of the MD runs were excluded from this analysis. Energies were scaled relative to the pumped mode energy $k_B T_{\text{pump}}$ in the initial state, such that the first energy in each time series $E_1 \approx 1$. When modeling the sum of energies of the two degenerate TO modes, the substitutions $T_{\text{eq}} \rightarrow 2T_{\text{eq}}$ and $T_{\text{pump}} \rightarrow T_{\text{pump}} + T_{\text{eq}}$ were made to account for the higher equilibrium energy. Secondly, in order to reduce correlations between data points close in time, block averaging was used. The 10 000 energy data points $E_n = E(t_n)$ where split into 100 blocks of consecutive values, which were then averaged to attain the block energies $E_{b,i} = E_b(t_{b,i})$, where $t_{b,i} = t_{n=100i}$ is the time coordinate of the start of the block. The block energy variances were calculated using

$$Var(X) = \overline{X^2} - \overline{X}^2,$$

where $\overline{X}$ denotes the mean of the random variable X. This was done by using the fully time resolved energy means $E_n = (\overline{E})_n$ and variances $\sigma_n^2 = Var(E)_n$ to calculate $(\overline{E^2})_n$, block averaging this quantity to get $(\overline{E_b^2})_i$, and subtracting the squared block averaged energies $(E_b^2)_i = (\overline{E_b})_i^2$.

Energies were modeled using three parameters,

$$E_m(t_n; \tau, E_{\text{pump}}, E_{\text{eq}}) = (E_{\text{pump}} - E_{\text{eq}})e^{-t_i/\tau} + E_{\text{eq}},$$

Table 3.2: Gamma prior parameters.

	τ (TO)	τ (LA)	σ	E_{eq}
mode	40	10	$\left(\sum_{i=1}^{100} \frac{1}{\sigma_i^2}\right)^{-1/2}$	$\frac{T_{\text{eq}}}{T_{\text{pump}}}$
variance	50^2	5^2	0.1^2	$\left(\frac{T_{\text{eq}}}{2T_{\text{pump}}}\right)^2$

where E_m is the model energy, τ is the relaxation time, E_{pump} is the initial energy of the pumped mode and E_{eq} is the equilibrium energy, i.e., the average energy of the pumped mode after relaxation. The block averaging was accounted for by the inclusion of a correction factor derived by block averaging the exponential model

$$\Lambda = \frac{1}{100} \frac{e^{-100\Delta t/\tau} - 1}{e^{-\Delta t/\tau} - 1},$$

where $\Delta t = 0.02$ (0.002) for the TO (LA) mode. The model for block averaged energies was thus

$$E_{b,m}(t_{b,i}; \tau, E_{\text{pump}}, E_{\text{eq}}) = \Lambda(E_{\text{pump}} - E_{\text{eq}})e^{-t_i/\tau} + E_{\text{eq}}.$$

Deviations in the data from the model were, in turn, modeled using a weighted multivariate normal distribution with an error scale parameter σ and with a weight matrix derived from the block variances σ_i^2,

$$W_{ij} = \frac{\frac{1}{\sigma_i^2}}{\sum_{i=1}^{100} \frac{1}{\sigma_i^2}} \delta_{ij}.$$

Here, the weight matrix is diagonal as indicated by the Kronecker delta, and normalized such that $Tr(W) = 1$. The data likelihood was thus described by

$$p(\boldsymbol{E}_d | \tau, \sigma, E_{\text{pump}}, E_{\text{eq}}) = \frac{|W|^{1/2}}{(2\pi\sigma^2)^{100/2}} \exp\left(-\frac{(\boldsymbol{E}_d - \boldsymbol{E}_{d,m})^T W (\boldsymbol{E}_d - \boldsymbol{E}_{d,m})}{2\sigma^2}\right).$$

For τ, σ and E_{eq}, Gamma distribution priors were used, with parameters chosen by selecting physically motivated modes and variances for the distributions, and from them deriving the shape parameters. For E_{pump}, a normal distribution was used as the prior, with mean 1 and standard deviation $T_{\text{eq}}/T_{\text{pump}}$. The Gamma prior modes and variances are shown in Table 3.2. Finally, the posterior was sampled using the `EnsembleSampler` in the EMCEE package [16], with 1000 burn-in steps, 4000 production steps and 8 walkers. The number of posterior samples was verified to be greater than or close to 50 times the sample autocorrelation times, in accordance with EMCEE documentation, and the acceptance rate was about 0.6 for all runs.

Figure 3.9 shows the results of the Bayesian modeling at $T_{\text{eq}} = 300\,\text{K}$, where the medians of the model posteriors are illustrated by dashed black lines along with the underlying data as solid purple lines. It is evident that the exponential model does not capture the full behavior of the relaxation. As the pumping temperature increases, an oscillatory component in the decaying mode energy becomes increasingly
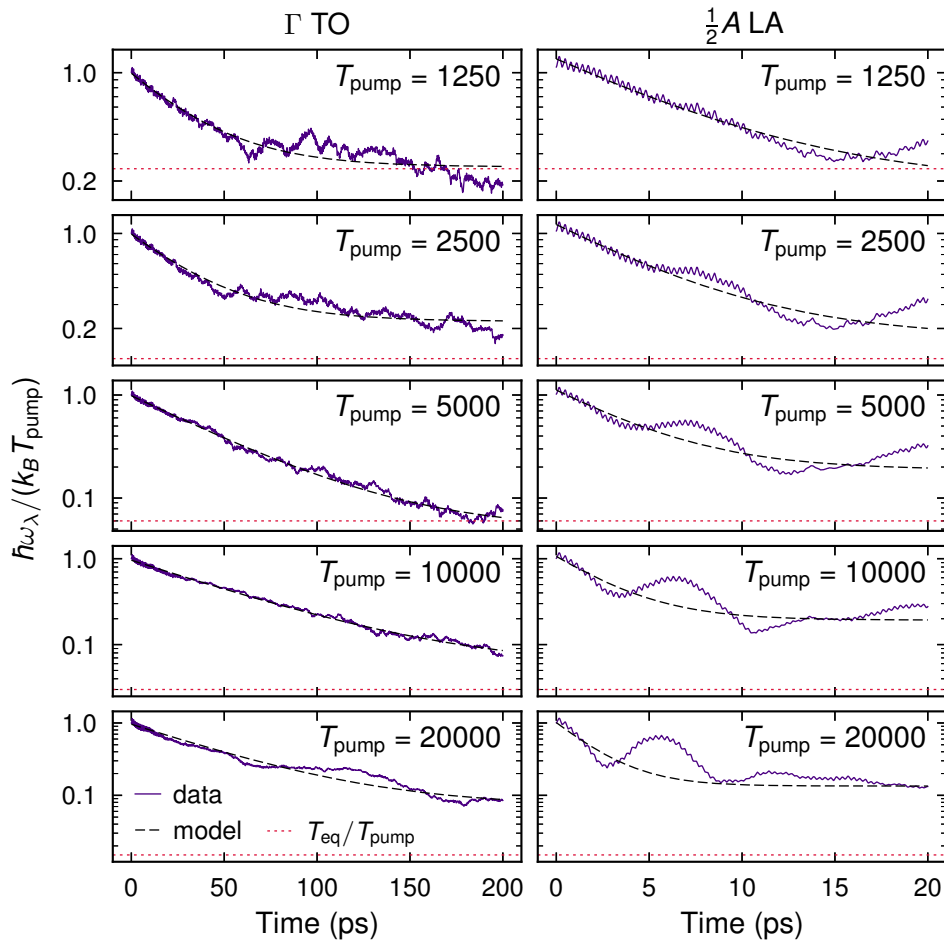
Figure 3.9: Exponential models for the energy of pumped modes Γ TO and $\frac{1}{2}A$ LA at a background temperature of $T_{\mathrm{eq}} = 300\,\mathrm{K}$ and effective pumping temperatures of $1250\,\mathrm{K}$, $2500\,\mathrm{K}$, $5000\,\mathrm{K}$, $10\,000\,\mathrm{K}$ and $20\,000\,\mathrm{K}$. The dashed black lines show the median of the model posteriors, fitted to the MD data, in turn shown as solid purple lines. The background temperature is indicated as dotted red lines, and all values are shown normalized to the pumping temperatures.

apparent, see subsection 3.5.2 for details. Furthermore, although the exponential model seems to extract the sought relaxation times at a low pumping temperature ($T_{\mathrm{pump}} = 1250\,\mathrm{K}$), this is not the case when the system is driven farther from equilibrium. Instead, the exponential models plateau at temperature far above the actual background temperature, and so the extracted relaxation time does not measure the time taken for the system to return to equilibrium, but rather to reach the plateau. This is at least partially a size effect caused by the moderate simulation cell size, and is discussed in more detail in the following section.

3.5.2 Longitudinal Acoustic mode pumping

Figure 3.10 shows how the energy is distributed from the pumped $\frac{1}{2}A$ ($\boldsymbol{q} = [0, 0, 1/4]$) LA mode into other modes along the ΓA band at a pumping temperature of $T_{\mathrm{pump}} =$
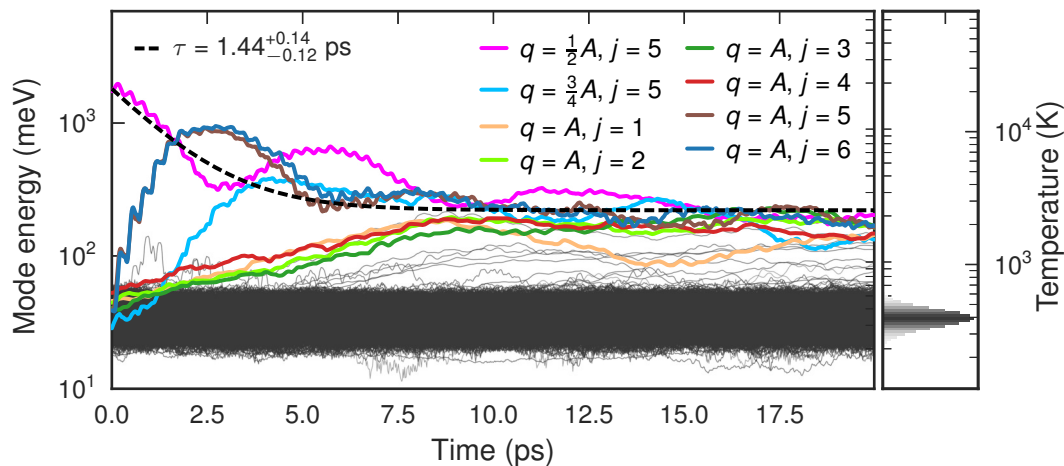
Figure 3.10: Phonon energy over time after pumping the LA mode halfway between Γ and A ($\boldsymbol{q} = [0, 0, 1/4]$) to an effective temperature of $T_{\text{pump}} = 20\,000\,\text{K}$ from an equilibrium temperature of $T_{\text{eq}} = 400\,\text{K}$.

$20\,000\,\text{K}$. The pumped mode seems most strongly coupled to the degenerate LA and longitudinal optical (LO) modes ($j = 5$ and $j = 6$) at A, since these are the first modes that are excited as the pumped mode decays. Energy even seems to oscillate back and forth between the $\frac{1}{2}A$ LA mode and the two A modes with a period time of about $5.5\,\text{ps}$ (equivalent to $0.18\,\text{THz}$). Shorter oscillations are also present in these modes, with a period of about $0.25\,\text{ps}$ (equivalent to $4.0\,\text{THz}$) for the pumped mode, but are most likely caused by calculating the mode energies using the harmonic frequencies, rather than the renormalized ones. Energy oscillating back and forth between modes is, however contrary both to the RTA and to the exponential model. On the other hand, the strong coupling between these modes is consistent with Fermi's golden rule and the scattering described in Eq. (2.26), with λ representing either of the A modes and $\lambda' = \lambda''$ both being the pumped mode. In other words, pairs of pumped mode phonons scatter to form A LA and LO phonons, conserving crystal momentum. Comparing with Figure 3.8, it is clear the total energy is also conserved, as all three (two degenerate) acoustic bands between Γ and A are almost completely linear. After about $2.5\,\text{ps}$, the $\frac{3}{4}A$ ($\boldsymbol{q} = [0, 0, 3/8]$) LA mode ($j = 5$) is significantly excited. This energy transfer, however, is not well explained by Eq. (2.26), even when taking into account scattering between the pumped mode and the two excited A modes. The only three-phonon interaction that includes the $\frac{1}{2}A$ and $\frac{3}{4}A$ modes and conserves crystal momentum is the one where a single $\frac{1}{2}A$ mode decays into two $\frac{3}{4}A$ phonons, but this would violate energy conservation. Energy is rather most likely transferred to the $\frac{3}{4}A$ mode through a higher-order interaction such as the one where a $\frac{1}{2}A$ and an A phonon scatter to form two $\frac{3}{4}A$ phonons. This would explain the delay in the excitation of the $\frac{3}{4}A$ mode, as the scattering cannot occur to a significant degree until the A modes are excited. At around $5\,\text{ps}$ four more modes are distinctly out of equilibrium. All four modes are at the A point and degenerate, with two being TA ($j = 1, 2$) and the other two being TO ($j = 3, 4$). Again, the interaction is not perfectly explained by Eq. (2.26), as
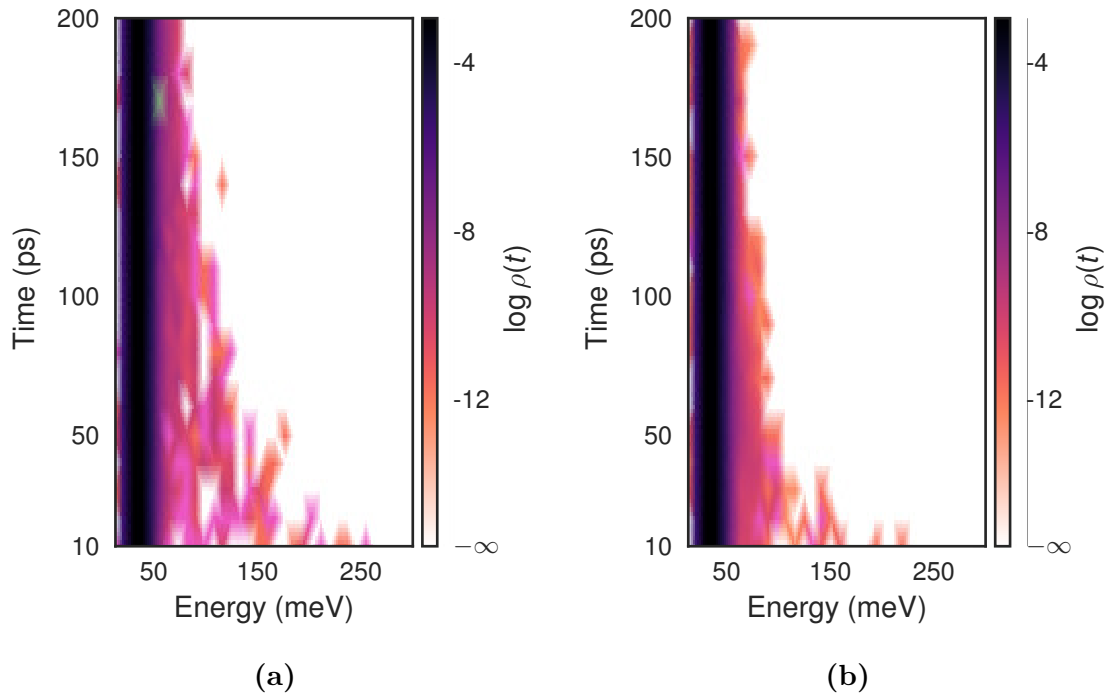
Figure 3.11: Energy density as a function of time after pumping the LA mode halfway between Γ and A ($q = [0, 0, 1/4]$) to an effective temperature of $T_{\text{pump}} = 20\,000$ K from an equilibrium temperature of $T_{\text{eq}} = 400$ K. The simulated supercell is a $12 \times 12 \times 8$ repeated graphite unitcell in (a), and a $12 \times 12 \times 16$ repeated unitcell in (b).

a pair of $\frac{1}{2}A$ phonons scattering into one of the four modes would merely conserve momentum but not energy. A single A LA phonon has a bit more than twice the energy of the four modes, but if the band linewidths are large enough this might be the most probable scattering path. Taking into account four-phonon processes, a similar path might be available if two $\frac{1}{2}A$ phonons scatter and form two TA or TO phonons at A. Finally, a single A LA phonon could decay into three phonons in the lower bands if linewidths are large enough.

More modes start getting excited after about 7.5 ps, likely due to scattering involving the hitherto latest excited transversal A modes. Instead of further examining the scattering details, it is at this point more interesting to consider the situation at around 10 ps and onward. The pumped mode seems to have stabilized in an excited state, with the exponential fit leveling out at a background temperature of about 2500 K. Similarly, the other excited modes level out and seem to remain out of equilibrium for a long time. This phenomenon could be explained by the collection of excited modes being in a quasi-equilibrium, where scattering between excited modes merely moves energy around within the collection, and interactions are rare that leak energy to the rest of the system.

Figure 3.11a shows the phonon energy density across all modes as a function of time up to $t = 200$ ps, with the same initial state as in Figure 3.10, but with a time resolution of 10 ps. The quasi-equilibrium persists for a rather long time, as the system still has not fully relaxed after 200 ps, indicating a collective lifetime far

above the exponentially fitted $\tau = 1.44^{+0.14}_{-0.12}$ ps. This is, however, partially caused by the finite size of the simulation cell, as can be seen by comparing Figs. 3.11a and 3.11b. The left and right figures show the time evolution when the simulated supercell comprises $12 \times 12 \times 8$ and $12 \times 12 \times 16$ unitcells, respectively. Since the latter systems is twice as large in the out-of-plane direction, the reciprocal lattice $\boldsymbol{q}$ resolution is twice as high between Γ and A, meaning more phonon modes are available for scattering. As a result, the quasi-equilibrium relaxes faster in the larger simulation cell, albeit still slower than the initial exponential fit would indicate. Investigating whether and when this size dependence converges is beyond the scope of this work, but should be the subject of future research.

3.5.3 Transversal optical mode pumping

Figure 3.12 shows how the energy is distributed among phonon modes after pumping one of two degenerate TO modes ($j = 4$) at Γ to an effective temperature of 5000 K from equilibrium temperatures of (a) 300 K and (b) 400 K. The situation here is considerably simpler than when pumping the LA mode. Most of the pumped energy simply transfers to the unpumped degenerate mode ($j = 5$), and no other modes are significantly excited. This result is somewhat unexpected, as three other modes seem reachable via third-order scattering according to Eq. (2.26), namely the $\boldsymbol{q} = \pm[0, 0, 1/8]$ LA mode and $\boldsymbol{q} = \pm[0, 0, 3/8]$ TA modes (twice degenerate). Looking at Fig. 3.8, energy and crystal momentum could be conserved when a single Γ TO phonon decays into one $+\boldsymbol{q}$ and one $-\boldsymbol{q}$ phonon of either of these modes. Since neither of these modes are excited in Fig. 3.12, the third-order force constants for these interactions are likely small. The most prominent fourth-order interaction is with the $\boldsymbol{q} = \pm[0, 0, 1/4]$ TO mode, where two Γ TO phonons scatter under formation of one $+\boldsymbol{q}$ and one $-\boldsymbol{q}$ TO phonons. This mode is faintly visibly excited to an effective temperature of about 500 K as a thin gray line in Fig. 3.12a between $t = 50$ ps and $t = 125$ ps.

Comparing the two figures, the excited modes relax faster when the background temperature is higher. This is expected, as a higher background is equivalent to higher average occupation numbers for all modes, which in turn increases all scattering rates. Although weak, the two excited modes lose energy to the rest of the system through higher-order scattering interactions, which nevertheless happens more frequently at higher temperatures. The consequence is a temperature dependence in the pumped relaxation time τ.

The simplicity of the situation facilitates a straightforward analysis of the quasi-equilibrium model introduced in the previous section. Since the two degenerate TO modes can be considered to compose the full collective excitation, the sum of their energies is the energy of the collective mode. This sum is illustrated in Fig. 3.12 as the light orange lines. Exponential fits to this energy sum are also shown, and the extracted relaxation times of the collective excitation are significantly longer than those of the pumped mode, at both background temperatures. This gives credence to the quasi-equilibrium model, and suggests a similar analysis could be done for more complicated relaxation paths, if all substantially excited modes are included in the sum. Such an analysis is another potential target for future work. Rather than

performing full pumped MD simulations to find which modes should be included in a particular collective excitation, the third-order force constants in Eq. (2.26) could likely be analyzed to find groups of phonon modes which are coupled strongly internally, and weakly externally.
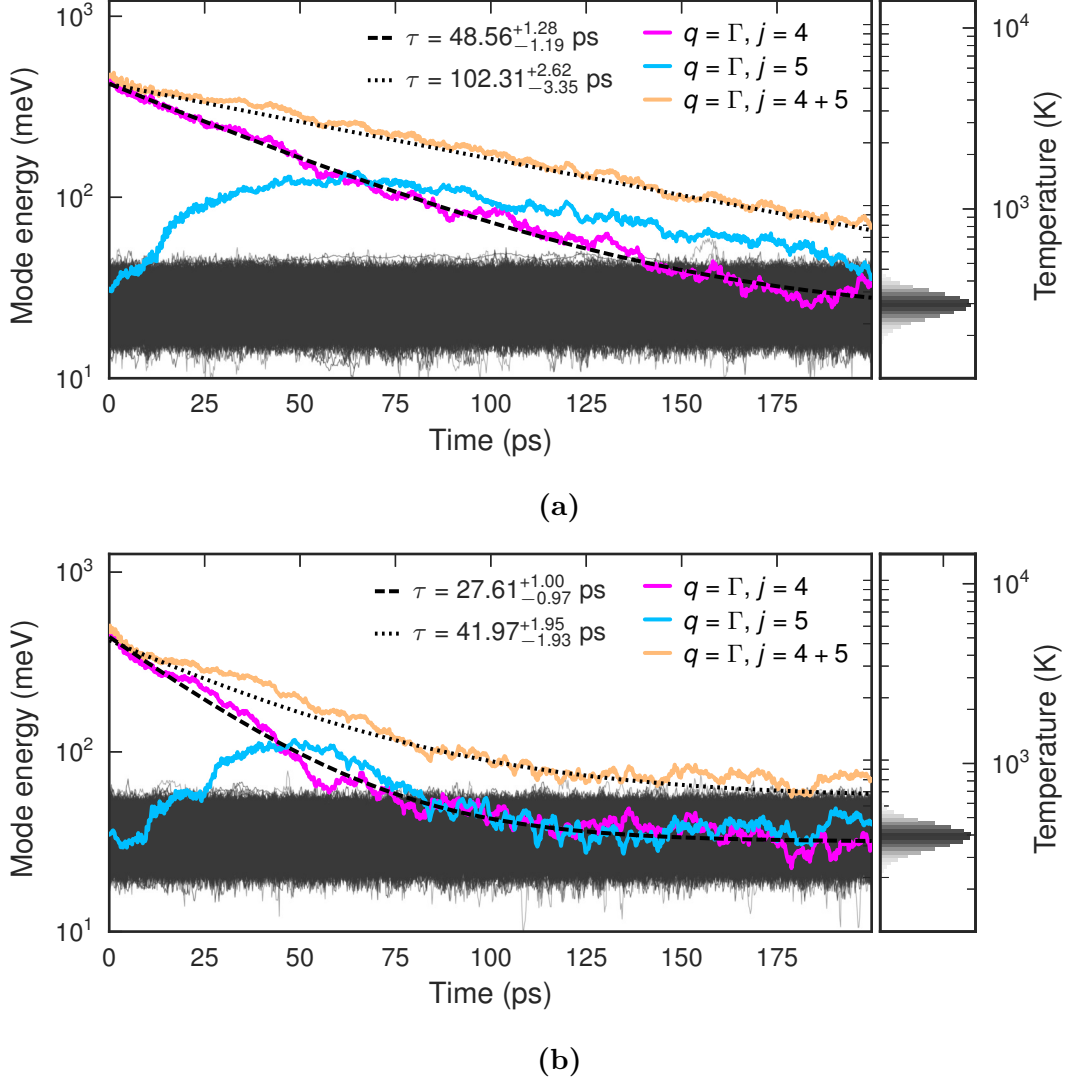

(a)

(b)

Figure 3.12: Phonon energy over time after pumping the TO mode halfway at Γ to an effective temperature of $T_{\text{pump}} = 5000\,\text{K}$ from equilibrium temperatures of $T_{\text{eq}} = 300\,\text{K}$ (a) and $T_{\text{eq}} = 400\,\text{K}$ (b).

3.5.4 Non-equilibrium lifetimes

Figure 3.13 shows the median posterior lifetimes extracted via Bayesian modeling for the two pumped modes, at background temperatures of $300\,\text{K}$ (purple lines) and $400\,\text{K}$ (red lines) as a function of pumping temperature. The dashed lines in the upper figure shows the lifetimes of the composite mode, modeled as the sum of energies of the two degenerate Γ TO modes. Additionally, the figure shows
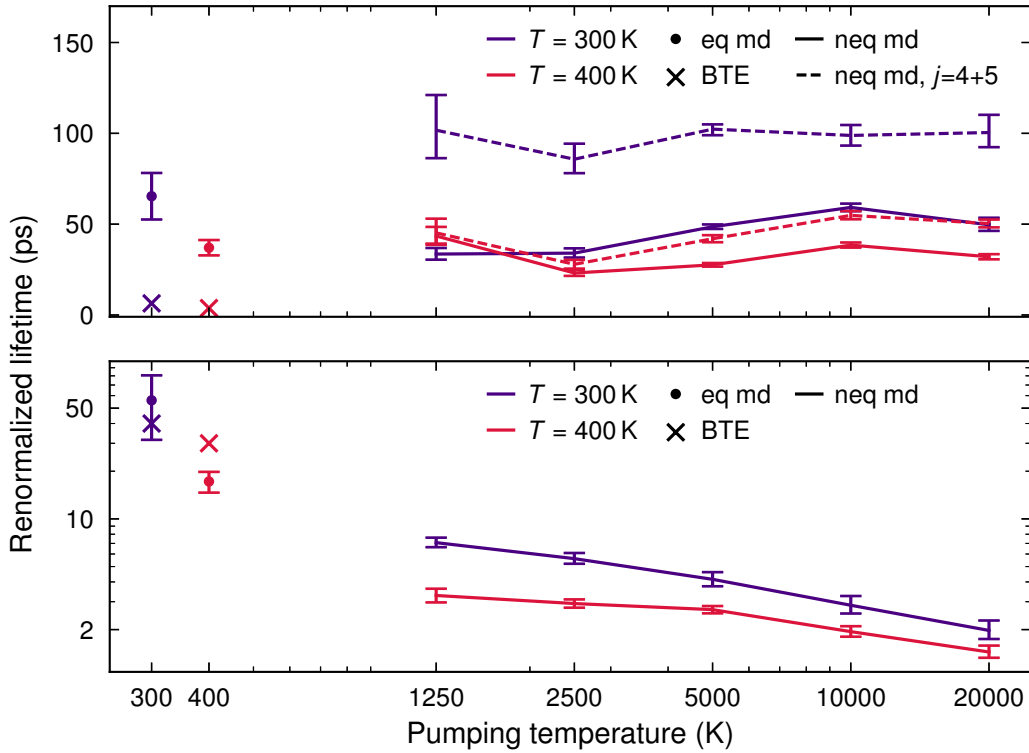
Figure 3.13: Pumped mode lifetimes as a function of pumping temperature for Γ TO and $\frac{1}{2}A$ LA at background temperatures of $300\,\mathrm{K}$ (purple lines) and $400\,\mathrm{K}$ (red lines). Equilibrium lifetimes are shown as dots with error bars (calculated from equilibrium MD) and as crosses without error bars (calculated by numerically solving the LBTE). The equilibrium MD error bars show one standard deviation and the non-equilibrium MD error bars show the 5th and 95th percentiles. In the upper figure, the dashed lines show the non-equilibrium lifetimes of the composite mode consisting of the two degenerate Γ TO modes.

the equilibrium lifetimes calculated via autocorrelation analysis of equilibrium MD phonon momenta (dots with error bars), and by numerically solving the LBTE using PHONO3PY [29] (crosses without error bars). When solving the LBTE, a system size of $30 \times 30 \times 10$ unitcells was used [11], giving a resolution in reciprocal space of 6 $\boldsymbol{q}$-points between the Γ and A points, inclusive. The error bars for the autocorrelation lifetimes show one standard deviation, extracted as the square root of the lifetime variance in the covariance matrix returned by `curve_fit` used as described in section 3.4. As for the non-equilibrium lifetimes, the errors bars instead show the 5th and 95th percentiles of the lifetime posteriors from the Bayesian modeling. Note that these errors show the uncertainty in the lifetime under the assumption that the energies relax exponentially. As can be seen in Fig. 3.9, this assumption is flawed, and as such the lifetime uncertainties should be interpreted carefully. Furthermore, the exponential model lifetimes themselves measure the time for the pumped mode to reach quasi-equilibrium and not true equilibrium, especially at higher pumping temperatures. This effect is more pronounced for the LA mode, as can be seen in Fig. 3.9, because quasi-equilibrium is reached quickly but relaxes

to true equilibrium slowly. A likely explanation is simply the fact that more modes are part of the collective excitation for the LA mode than for the TO mode. Hence, the initially pumped LA mode has more paths available to distribute its energy to the other modes in the quasi-equilibrium.

Some patterns can be identified in Fig. 3.13. For the TO mode, the lifetime dependence on pumping temperature is weak or nonexistent, but the lifetimes of the composite mode are consistently higher than the one of the pumped mode alone. Furthermore, this effect is more pronounced at the lower background temperature. A probable explanation is that, once both degenerate modes are excited, the scattering rate between them is independent of the background temperature, while the scattering rate to other modes increases with the background temperature. The relative rate of external scattering compared to internal scattering of the composite mode therefore increases with the background temperature, causing the composite mode to relax faster.

As for the LA mode, there is a clear negative dependence of the lifetime on the pumping temperature. In other words, quasi-equilibrium is reached faster at higher pumping temperatures. This can be explained by the fact that scattering rates between strongly coupled modes increase the occupations of the scattering modes. A higher initial energy of the pumped mode would more quickly excite strongly coupled modes, which would in turn further increase scattering rates out of the pumped mode.

The decreasing relaxation time to quasi-equilibrium is probably in contrast to the relaxation time to true equilibrium, which is expected to show the opposite behavior, as more energy in the collective excitation should take longer to dissipate to the rest of the system. This expectation is motivated by the fact that the collective excitation is, by definition, more weakly coupled to other modes, and so higher pumping temperatures should increase internal scattering while barely affecting external scattering. At the least, this is expected to be the case as long as the modes are not driven out of equilibrium, i.e., as long as the rest of the system behaves as a heat bath of constant temperature. If external modes are driven out of equilibrium the external scattering rate would increase and the quasi-equilibrium lifetime decrease, meaning there must be a pumping temperature at which the lifetime is maximized.

4

Conclusions

In this work, the details of thermal transport in vdW thin film stacks have been investigated by studying phonon modes important for the LTC, using graphite as a prototype material.

The goal of finding an optimal twist angle for maximizing the LTC anisotropy has not been reached, as time-consuming obstacles were reached when attempting to perform MD simulations and phonon mode projection of moiré structures. When performing MD simulations of twisted structures using similar supercell sizes as for regular graphite, individual atomic films randomly drifted in the in-plane directions. This happened to such a degree that the harmonic approximation of the potential energy completely failed, as atoms ended up further from their own equilibrium positions than from those of other atoms. Two potential fixes exist, both of which were too inefficient to use. Firstly, the atoms could be re-indexed in each time step of the MD simulation so the index of each atom matches the index of the nearest possible equilibrium position. This is an example of the linear assignment problem, which is solvable in polynomial time in the number of atoms [9], and an implementation using SCIPY turned out to be unfeasibly slow. The other, preferable, solution would be to use a larger simulation cell, which would cause performance and memory resource issues with the implementation of the dynamical matrix construction used in the present work. The size in memory of the full set of force constants used to calculate the dynamical matrix scales quadratically with the number of atoms in the supercell. This could be substantially reduced by keeping the sparse representation used in HIPHIVE as force constants between atoms far apart are practically zero. In the present work, however, fully dense force constant arrays were used for ease of implementation. The performance issue was caused by using a naive implementation for calculating the Fourier transformed FCs, with a scaling of at least $\mathcal{O}(N^3)$ in the number of atoms. Using the Fast Fourier Transform algorithm instead, it would be possible to bring this scaling down to $\mathcal{O}(N^2 \log N)$ or $\mathcal{O}(N \log N)$, which would enable using vastly larger system sizes.

Another goal was explaining the extreme anisotropy in the thermal conductivity of twisted stacks, which was for similar reasons not directly investigated. Indirectly, however, the investigation of out-of-plane phonon modes in graphite can be used to predict the mechanism of thermal transport in the twisted structures. Since the LA band is predicted to dominate though-plane heat conduction and is almost identical between graphite and the first moiré structure (see Fig. 3.5), the results found for graphite can provide some insight for the twisted structures as well. The non-equilibrium MD simulations where the $\frac{1}{2}A$ LA mode was pumped (see Fig. 3.10) showed that the majority of scattering occurred within the LA band, with modes

in the TA band only joining in via rare fourth-order interactions. Furthermore, the scattering was initially dominated entirely by the two degenerate LA and LO modes at A. This could be expected to match the situation in equilibrium, since the observed scattering to other modes only occurred once the initial two had been driven far from equilibrium. The concluding prediction for the simplest twisted structure, then, is that the lifetimes of LA modes, and hence likewise the though-plane thermal conductivity, should largely be the same as in graphite. For smaller twist angles, however, Fig. 3.6 gives a different idea. Although the acoustic mode itself remains largely unchanged as the twist angle decreases, optical modes appear in greater numbers and gradually inches closer in energy to the LA mode. If out-of-plane LA phonons in twisted structures still predominantly scatter with other modes between Γ and A, these adjacent optical bands could provide new relaxation pathways. This would, as predicted, decrease the LA phonon lifetimes, which would in turn explain the low through-plane thermal conduction observed in [19]. Running mode pumping simulations for twisted structures with small twist angles would potentially be able to confirm or disprove these suspicions.

The third and final objective was to explore the limitations of the RTA to describe the LTC of thin vdW stacks. This was accomplished with the mode pumping simulations, as pushing even a single mode in the system far from equilibrium was enough to invoke behavior at odds with the RTA. Perhaps the most obvious example is Fig. 3.9, where the RTA would predict exponential curves akin to the dashed lines in the figure. Instead, the observed relaxation curves deviate from this prediction progressively as the effective pumping temperature increases, and even display oscillatory behavior. This can be understood by examining Fig. 3.10, in which it is evident the energy, rather than dissipating to the rest of the system, oscillates back and forth between a few strongly coupled modes. The other, potentially more interesting, observed violation of the RTA is the formation of a long-lived quasi-equilibrium state visible in Figs. 3.10 and 3.11. As the quasi-equilibrium lifetime was observed to be size-dependent, more work is needed to determine when this size-dependence converges. If the effect persists in large enough crystals, it might be possible to experimentally verify by the following method. The particular quasi-equilibrium observed here consisted largely of out-of-plane modes contributing to the LTC. Hence, if the mode pumping simulations are emulated experimentally by the excitation via laser of the same modes, it should be possible to observe an increased out-of-plane LTC. Tuning of the laser and measuring the decay time of the increased thermal conductivity would be a direct measurement of the quasi-equilibrium lifetime. Furthermore, varying the amplitude of the laser would affect the quasi-equilibrium temperature and hence also the LTC. Below a certain limit, amplitudes would not be enough to create a quasi-equilibrium, so the LTC dependence on amplitude below and above this limit should be characteristically different. Progressively increasing the amplitude from zero and observing whether the thermal conductivity shows such a change in characteristics would thus be a way to test whether a quasi-equilibrium forms.

Bibliography

[1]   J. Ajayan et al. "Nanosheet Field Effect Transistors-A next Generation Device to Keep Moore's Law Alive: An Intensive Study". In: *Microelectronics Journal* 114 (Aug. 2021), p. 105141. ISSN: 0026-2692. DOI: `10.1016/j.mejo.2021.105141`.

[2]   Kristian Berland and Per Hyldgaard. "Exchange Functional That Tests the Robustness of the Plasmon Description of the van Der Waals Density Functional". In: *Physical Review B* 89.3 (Jan. 2014), p. 035412. DOI: `10.1103/PhysRevB.89.035412`.

[3]   Efrem Braun, Seyed Mohamad Moosavi, and Berend Smit. "Anomalous Effects of Velocity Rescaling Algorithms: The Flying Ice Cube Effect Revisited". In: *Journal of Chemical Theory and Computation* 14.10 (Oct. 2018), pp. 5262–5272. ISSN: 1549-9618. DOI: `10.1021/acs.jctc.8b00446`.

[4]   Joakim Brorsson et al. "Efficient Calculation of the Lattice Thermal Conductivity by Atomistic Simulations with Ab Initio Accuracy". In: *Advanced Theory and Simulations* n/a.n/a (2021), p. 2100217. ISSN: 2513-0390. DOI: `10.1002/adts.202100217`.

[5]   Giovanni Bussi, Davide Donadio, and Michele Parrinello. "Canonical Sampling through Velocity Rescaling". In: *The Journal of Chemical Physics* 126.1 (Jan. 2007), p. 014101. ISSN: 0021-9606. DOI: `10.1063/1.2408420`.

[6]   Giovanni Bussi and Michele Parrinello. "Accurate Sampling Using Langevin Dynamics". In: *Physical Review E* 75.5 (May 2007), p. 056707. DOI: `10.1103/PhysRevE.75.056707`.

[7]   *calorine - A Python tool box for GPUMD simulations*. URL: `https://calorine.materialsmodeling.org/index.html` (visited on 10/03/2022).

[8]   Laurent Chaput et al. "Phonon-Phonon Interactions in Transition Metals". In: *Physical Review B* 84.9 (Sept. 2011), p. 094302. DOI: `10.1103/PhysRevB.84.094302`.

[9]   David F. Crouse. "On implementing 2D rectangular assignment algorithms". In: *IEEE Transactions on Aerospace and Electronic Systems* 52.4 (2016), pp. 1679–1696. DOI: `10.1109/TAES.2016.140952`.

[10]   M. Dion et al. "Van der Waals Density Functional for General Geometries". In: *Physical Review Letters* 92.24 (June 2004), p. 246401. DOI: `10.1103/PhysRevLett.92.246401`.

[11]   Paul Erhart, Erik Fransson, and Fredrik Eriksson. *Private communication.* 2022.

[12]   Fredrik Eriksson, Erik Fransson, and Paul Erhart. "The Hiphive Package for the Extraction of High-Order Force Constants by Machine Learning". In: *Advanced Theory and Simulations* 2.5 (2019), p. 1800184. ISSN: 2513-0390. DOI: `10.1002/adts.201800184`.

[13]   Zheyong Fan et al. "Efficient Molecular Dynamics Simulations with Many-Body Potentials on Graphics Processing Units". In: *Computer Physics Communications* 218 (Sept. 2017), pp. 10–16. ISSN: 0010-4655. DOI: `10.1016/j.cpc.2017.05.003`.

[14]   Zheyong Fan et al. "Neuroevolution machine learning potentials: Combining high accuracy and low cost in atomistic simulations and application to heat transport". In: *Physical Review B* 104 (10 Sept. 2021), p. 104309. DOI: `10.1103/PhysRevB.104.104309`.

[15]   M. Fechner and N. A. Spaldin. "Effects of Intense Optical Phonon Pumping on the Structure and Electronic Properties of Yttrium Barium Copper Oxide". In: *Physical Review B* 94.13 (Oct. 2016), p. 134307. DOI: `10.1103/PhysRevB.94.134307`.

[16]   Daniel Foreman-Mackey et al. "emcee: The MCMC Hammer". In: *Publications of the Astronomical Society of the Pacific* 125.925 (Mar. 2013), p. 306. DOI: `10.1086/670067`. arXiv: `1202.3665 [astro-ph.IM]`.

[17]   Erik Fransson et al. "dynasor—A Tool for Extracting Dynamical Structure Factors and Current Correlation Functions from Molecular Dynamics Simulations". In: *Advanced Theory and Simulations* 4.2 (2021), p. 2000240. DOI: `https://doi.org/10.1002/adts.202000240`. eprint: `https://onlinelibrary.wiley.com/doi/pdf/10.1002/adts.202000240`. URL: `https://onlinelibrary.wiley.com/doi/abs/10.1002/adts.202000240`.

[18]   Klaus Hermann. "Periodic Overlayers and Moiré Patterns: Theoretical Studies of Geometric Properties". In: *Journal of Physics: Condensed Matter* 24.31 (July 2012), p. 314210. ISSN: 0953-8984. DOI: `10.1088/0953-8984/24/31/314210`.

[19]   Shi En Kim et al. "Extremely Anisotropic van Der Waals Thermal Conductors". In: *Nature* 597.7878 (Sept. 2021), pp. 660–665. ISSN: 1476-4687. DOI: `10.1038/s41586-021-03867-8`.

[20]   Ask Hjorth Larsen et al. "Libvdwxc: A Library for Exchange–Correlation Functionals in the vdW-DF Family". In: *Modelling and Simulation in Materials Science and Engineering* 25.6 (June 2017), p. 065004. ISSN: 0965-0393. DOI: `10.1088/1361-651X/aa7320`.

[21]   Ask Hjorth Larsen et al. "The Atomic Simulation Environment—a Python Library for Working with Atoms". In: *Journal of Physics: Condensed Matter* 29.27 (June 2017), p. 273002. ISSN: 0953-8984. DOI: `10.1088/1361-648X/aa680e`.

[22]   Yao-Jen Lee et al. "Ge GAA FETs and TMD FinFETs for the Applications Beyond Si—A Review". In: *IEEE Journal of the Electron Devices Society* 4.5 (Sept. 2016), pp. 286–293. ISSN: 2168-6734. DOI: 10.1109/JEDS.2016.2590580.

[23]   Glenn J. Martyna, Michael L. Klein, and Mark Tuckerman. "Nosé–Hoover Chains: The Canonical Ensemble via Continuous Dynamics". In: *The Journal of Chemical Physics* 97.4 (Aug. 1992), pp. 2635–2643. ISSN: 0021-9606. DOI: 10.1063/1.463940.

[24]   Arden L. Moore and Li Shi. "Emerging Challenges and Materials for Thermal Management of Electronics". In: *Materials Today* 17.4 (May 2014), pp. 163–174. ISSN: 1369-7021. DOI: 10.1016/j.mattod.2014.04.003.

[25]   Murali Gopal Muraleedharan et al. "Understanding Phonon Transport Properties Using Classical Molecular Dynamics Simulations". In: *arXiv:2011.01070 [cond-mat]* (Nov. 2020). arXiv: 2011.01070 [cond-mat].

[26]   Michele Simoncelli, Nicola Marzari, and Francesco Mauri. "Unified Theory of Thermal Transport in Crystals and Glasses". In: *Nature Physics* 15.8 (Aug. 2019), pp. 809–813. ISSN: 1745-2481. DOI: 10.1038/s41567-019-0520-x.

[27]   William C. Swope et al. "A Computer Simulation Method for the Calculation of Equilibrium Constants for the Formation of Physical Clusters of Molecules: Application to Small Water Clusters". In: *The Journal of Chemical Physics* 76.1 (Jan. 1982), pp. 637–649. ISSN: 0021-9606. DOI: 10.1063/1.442716.

[28]   E. B. Tadmor et al. "Mixed Finite Element and Atomistic Formulation for Complex Crystals". In: *Physical Review B* 59.1 (Jan. 1999), pp. 235–245. DOI: 10.1103/PhysRevB.59.235.

[29]   Atsushi Togo, Laurent Chaput, and Isao Tanaka. "Distributions of Phonon Lifetimes in Brillouin Zones". In: *Physical Review B* 91.9 (Mar. 2015), p. 094306. DOI: 10.1103/PhysRevB.91.094306.

[30]   Atsushi Togo and Isao Tanaka. "First Principles Phonon Calculations in Materials Science". In: *Scripta Materialia* 108 (Nov. 2015), pp. 1–5. ISSN: 1359-6462. DOI: 10.1016/j.scriptamat.2015.07.021.

[31]   Atsushi Togo and Isao Tanaka. *Spglib: A Software Library for Crystal Symmetry Search*. Aug. 2018. DOI: 10.48550/arXiv.1808.01590. arXiv: 1808.01590 [cond-mat].

[32]   John M. Ziman. *Electrons and Phonons: the theory of transport phenomena in solids*. International series of monographs on physics (Oxford). Clarendon Press, 1960.

Bibliography